Defect-mediated Z-scheme BiO_{2-x}/$Bi_2O_{2.75}$ photocatalyst for full spectrum solar-driven organic dyes degradation

Min Wang[a], Guoqiang Tan[a,*], Dan Zhang[a], Bin Li[a], Long Lv[b], Ying Wang[a], Huijun Ren[c], XinLei Zhang[a], Ao Xia[a], Yun Liu[d]

[a] *Shaanxi Key Laboratory of Green Preparation and Functionalization for Inorganic Materials, School of Materials Science and Engineering, Shaanxi University of Science & Technology, Xi'an, 710021, China*
[b] *College of Cryptography Engineering, Engineering University of PAP, Xi'an, 710086, China*
[c] *School of Arts and Sciences, Shaanxi University of Science & Technology, Xi'an, 710021, China*
[d] *College of Electrical and Information Engineering, Shaanxi University of Science & Technology, Xi'an, 710021, China*

ARTICLE INFO

ABSTRACT

Defect-mediated Z-scheme BiO_{2-x}/$Bi_2O_{2.75}$ heterojunction photocatalysts without electron mediator was prepared via a simple low-temperature hydrothermal method. DFT proved that the existence of oxygen vacancies would affect the geometric and electronic structure of BiO_{2-x} and $Bi_2O_{2.75}$, which played an indispensable role in promoting exciton dissociation. BiO_{2-x}/$Bi_2O_{2.75}$ exhibited a higher redox ability compared with the pure BiO_{2-x} due to the Z-scheme photocatalytic mechanism, which could be ascribed to the formation of the build-in electric field induced by Bi and O defects. The as-synthesized photocatalysts exhibited excellent photocatalytic activity over the full solar spectrum from UV to NIR light due to the LSPR effect of oxygen vacancies, indicating its effective utilization of solar energy. The degradation rates of RhB over the optimal BiO_{2-x}/$Bi_2O_{2.75}$ were 8.49, 10.22 and 3.24 times higher than that of the pure BiO_{2-x} under visible light, simulated sunlight and NIR light irradiation, respectively. The excellent photocatalytic activity was ascribed to the synergistic effects of the LSPR effect of oxygen vacancies and the Z-scheme interfacial heterojunction. It was believed that this work provided a new idea to design high active and full solar spectrum-driven photocatalysts for energy conversion and environmental remediation.

1. Introduction

Over the past years, with the rapid development of economy and industrialization, the two severe crises of environmental pollution and energy shortage have generated tremendous attention [1–3]. Photocatalytic technology is regarded as an environmentally friendly and sustainable technology due to its potential application in environmental remediation and solar energy conversion by semiconductor-based photocatalysis [4–6].

Among conventional semiconductor materials, TiO_2 is considered as a promising photocatalyst due to its high reaction activity, excellent chemical ability and low-cost. Even so, the practical application of the TiO_2-based photocatalysts is limited because of its low utilization of solar light (4–5% UV light) and low quantum yield [7–10]. Recently, many researchers devote to explore visible-light-responsive photocatalysts. A large number of photocatalysts which can harvest UV–vis light have been reported, such as g-C_3N_4 [11–13], $BiVO_4$ [14,15],

Bi_2WO_6 [16,17], ZnS [18,19], MoS_2 [20,21] and Bi_2O_3 [22,23]. However, it is still difficult that photocatalytic reactions are performed by the NIR light which accounts for a fairly large proportion (about 50%) of solar spectrum [24–26]. To further improve the utilization of solar energy, much effort has been made to design and explore NIR-light-responsive photocatalysts. However, there are still many inherent drawbacks that limit their further development in the field of photocatalysis, including low redox ability, fast recombination of photoinduced charge carriers, narrow absorption range, low solar-chemical energy conversion efficiency and expensive price (narrow bandgap, up-conversion materials modified, noble metal deposition photocatalysts) [19,27–29]. In recent years, oxygen vacancy engineering has been become a research hotspot applying to the photocatalysts' modification [30]. According to the previous reports, oxygen vacancies can act as electrons trapping centers and active sites, which is beneficial to promoting the separation of the photoinduced electron-hole pairs and improving the absorption and activation ability for O_2 molecules [31].

Moreover, the electronic band structure of photocatalysts can be optimized by the localized electrons at oxygen vacancies [32]. Nevertheless, most of the oxygen vacancy-modified photocatalysts are synthesized by reduction methods in a harsh reaction condition [33,34]. Therefore, it is very vital for the development of a simple, facial and controllable method to prepare oxygen defect photocatalysts.

Oxygen vacancy-rich BiO_{2-x} nanosheets can be synthesized by a simple one-step hydrothermal, which exhibits satisfactory light absorption in the UV–vis-NIR range. The photocatalytic performance of BiO_{2-x} can be further improved by tuning thickness and Ni doping [35,36]. Moreover, semiconductor coupling is another effective modification strategy for BiO_{2-x} photocatalyst, which can improve the separation efficiency of the photogenerated charge carriers and inhibit the recombination of electron-hole pairs. A Z-scheme heterojunction of $Bi_2O_2CO_3$/graphene/BiO_{2-x} is constructed using graphene as electron mediator, which exhibits enhanced photocatalytic activity than that of $Bi_2O_2CO_3$, BiO_{2-x} and $Bi_2O_2CO_3$/BiO_{2-x} due to the promoted photo-induced charge carriers' separation and the strong redox ability [37]. Among the above BiO_{2-x}-based photocatalysts, the maximum absorption edge is located at 890 nm, which demonstrates that the solar energy is not fully utilized.

Hence, in this work, a series of oxygen vacancies induced Z-scheme BiO_{2-x}/$Bi_2O_{2.75}$ heterojunction photocatalysts with full solar spectrum response are prepared by a simple one-step hydrothermal route, which exhibit superior charge carrier separation efficiency, strong redox ability and high photocatalytic activity in visible-NIR range. In addition, the photocatalytic mechanism and the migration path of photo-induced electrons in the heterojunction interface are discussed according to the experimental results.

2. Experimental section

2.1. Preparation of BiO_{2-x}/$Bi_2O_{2.75}$

Typically, 1.8 mmol of $NaBiO_3$ powders were dispersed to 20 mL 3.0 M of NaOH aqueous solution to obtain a dark brown suspension after 30 min of magnetic stirring. Secondly, before-mentioned suspension was dispersed to 20 mL of deionized water slowly to obtain a suspension. Then, this suspension was transferred to Teflon vessel and heated at 180 °C for a certain time (20, 40, 60, 120 and 180 min). Finally, the precipitates were washed with deionized water and ethanol repeatedly and dried at 70 °C for 12 h. The samples with 20, 40, 60, 120 and 180 min reaction time were denoted as BiO-OVs-1, BiO-OVs-2, BiO-OVs-3, BiO-OVs-4 and BiO-OVs-5. The pure BiO_{2-x} was prepared when the reaction time was extended to 6 h.

Preparation of α-Bi_2O_3:α-Bi_2O_3 was prepared with $Bi(NO_3)_3$·$5H_2O$ as raw material under the same hydrothermal reaction conditions (180 °C, 40 min).

Preparation of β-Bi_2O_3: 6 mmol of $Bi(NO_3)_3$·$5H_2O$ and 5.7 mmol of citric acid were dispersed to 30 mL 1 M of HNO_3 aqueous solution under magnetic stirring. After that, 1 M of NaOH aqueous solution was dropwise added to the above solution to adjust the pH of the solution to ~4. The final solution was stirred for 30 min and then transferred to Teflon vessel and heated up to 180 °C for 24 h. $Bi_2O_2CO_3$ was obtained by washing and drying the product. β-Bi_2O_3 was prepared by calcining $Bi_2O_2CO_3$ at 300 °C for 2 h with the heating rate of 3 °C/min.

2.2. Characterization

The phase composition and crystal structure of all the samples were tested by the X-ray diffraction patterns (XRD, D/max-2200PC, Rigaku, Cu Kα, λ = 0.15406 nm, 40 kV, 40 mA) in the range of 25–70 ° and the laser micro-Raman spectroscopy (Raman, Renishaw invia, U.K., 532 nm excitation). The optical absorption properties of all the samples were reflected by UV–vis-NIR Diffuse Reflectance Spectra (DRS, Cray 500, Agilent, U.S.A) in the wavelength range of 200–2100 nm and $BaSO_4$

was used as the reference. The surface composition and chemical states were measured by X-ray photoelectron spectrometer (XPS, Model XSAM800, Shimadzu-Kratos Ltd., Japan). The morphologies of the as-prepared samples were observed by field emission scanning electron microscopy (SEM, FEI Verios 460) and transmission electron microscopy (TEM, FEI-Tecnai G2 F20). The concentration of total organic carbon (TOC) was determined by a TOC auto analyzer (Liqui TOC II). Electron paramagnetic resonance (EPR) signals were recorded with a Bruker a300 spectrometer to further detect the existence of oxygen vacancies as well as the formation of superoxide ($\cdot O_2^-$ in methanol solution) and hydroxide ($\cdot OH$ in aqueous solution) radicals in the photocatalytic reaction system with 5,5-dimethyl-1-pyrroline-Noxide (DMPO: 50 mM, 0.2 mL) as spin-trapped reagent at room temperature (25 °C) and an atmosphere. A 300 W Xe lamp with a 420 nm cut-off filter and 780 nm cut-off filter was used as visible and NIR light source, respectively. The external electromagnetic frequency was 9.875 GHz.

2.3. Computational details

In this work, density functional theory (DFT) calculations were carried out using the plane-wave pseudopotential and the Cambridge Sequential Total Energy Package (CASTEP) was used for calculation and analysis. The valence electron composition of atoms was selected as Bi $6s^26p^3$ and O $2s^22p^4$. The Perdew-Burke-Ernzerhof (PBE) of the generalized gradient approximation (GGA) was used to depict the exchange-correlation effects. The plane-wave cutoff energy was selected as 400 eV. The high symmetry in the form of special K points method of Monkorst-Packwas used for the integration of the Brillouin zone. The calculation accuracy was set to the total energy converges to 1×10^5 eV per atom and the convergence criterion of the force between atoms was 0.3 eV/nm. The maximum displacement was 2×10^4 nm and the maximum stress was 0.05 GPa.

2.4. Photocatalytic experiments

The photocatalytic activities of all the prepared samples in aqueous media were evaluated by the degradation of rhodamine B (RhB) under visible light (500 W xenon lamp with a UV-cutoff filter, $\lambda > 420$ nm), simulated sunlight (500 W xenon lamp, 190 nm < λ < 1100 nm) and NIR light irradiation (500 W xenon lamp with a filter, 800 nm < λ < 1500 nm), which was conducted in an XPA-7 photochemical reactor (Xujiang Machine Factory, Nanjing, China). Further, monochromatic photodegradation experiments with wavelength of 740 nm (5 W), 850 nm (5 W), 940 nm (5 W) and 1100 nm (5 W) were conducted to investigate the roles of the LSPR effect of oxygen vacancies. Typically, 50 mg of the prepared photocatalyst was suspended in 50 mL of RhB solution (5 mg/L) in a quartz tube and stirred for 30 min in darkness before illumination to achieve adsorption-desorption equilibrium between RhB molecules and photocatalysts. During photoreaction, 5 mL of the suspension was collected at a certain time and centrifuged (3500 rpm/min) for 15 min to remove the photocatalytic particles. The concentrations of RhB supernatant were measured using an UV–vis spectrophotometer (SP-756 P, Shanghai optical spectrometer company, China). The active species capture experiments were carried out by using benzoquinone(BQ), t-butanol (t-BuOH) and sodium oxalate ($Na_2C_2O_4$) as the scavengers for superoxide radical ($\cdot O_2^-$), hydroxyl radical ($\cdot OH$) and hole (h^+), respectively.

2.5. Photoelectrochemical measurement

The photoelectrochemical measurements were performed on an electrochemical workstation (CHI660E) in a standard three-electrode system with a platinum sheet as a counter electrode, a saturated Ag/AgCl electrode as a reference electrode and fluorine-doped tin oxide (FTO) conducting glass with as-prepared samples as working electrodes. The working electrodes were prepared as follows: Typically,
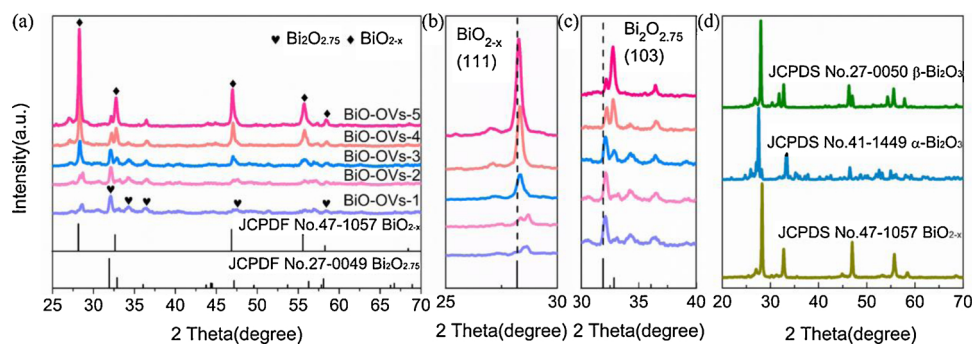
Fig. 1. (a) XRD patterns of BiO-OVs; magnified peaks in 2θ range (b) from 25° to 30°; (c) from 30° to 40°; (d) XRD patterns of pure BiO_{2-x}, α-Bi_2O_3 and β-Bi_2O_3.

0.02 g of photocatalyst was added into the mixed solution of 1 mL of absolute ethyl alcohol and 0.2 mL of film-forming reagent. After ultrasonic dispersion for 30 min, a homogeneous suspension was obtained. Then, the suspension was spread on the FTO glass and dried under ambient condition. A 500 W Xe arc lamp was used as the visible light source and 0.1 M of Na_2SO_4 aqueous solution was used as the electrolyte. The linear sweep voltammetry (LSV) and cyclic voltammetry (CV) were measured at a scan rate of 50 mV/s. The transient photocurrent response and electrochemical impedance spectroscopy (EIS) in the frequency of 0.01–100,000 Hz were performed under visible light irradiation. The EIS results were fitted by the ZsimpWin software.

3. Results and discussion

3.1. Structure, morphology and optical properties of $BiO_{2-x}/Bi_2O_{2.75}$ photocatalysts

XRD patterns were used to determine the phase composition and crystal structure of the BiO-OVs photocatalysts. As shown in Fig. 1(a), the diffraction peaks at 28.2°, 32.7°, 46.9°, 55.6° and 58.3° could be well-indexed with to (111), (200), (220), (311) and (222) crystal faces of the cubic phase BiO_{2-x} (JCPDS No.47-1057, space group: Fm-3 m, unit cell parameters: a = b = c = 0.5475 nm, α = β = γ = 90°). The peaks at 31.9°, 32.9°, 36.1°, 47.2° and 58.1° could be assigned to the (103), (110), (112), (200) and (213) crystal planes of the tetragonal phase $Bi_2O_{2.75}$ (JCPDS No.27-0049, space group: I4-3 m, unit cell parameter: a = b = 0.385 nm, c = 1.225 nm, α = β = γ = 90°). From the XRD patterns of BiO-OVs samples, the crystallinity of the samples and the content of BiO_{2-x} gradually increased as the reaction time was prolonged. It could be seen from Fig. 1(b) and (c) that the diffraction peaks of BiO_{2-x} and $Bi_2O_{2.75}$ slightly shifted compared with the standard cards, which originated from the existence of high concentrations of oxygen vacancies. In addition, the pure BiO_{2-x} was synthesized when the reaction time was lengthened to 6 h. It was well known that BiO_{2-x} and $Bi_2O_{2.75}$ belonged to deficient bismuth oxide. Therefore, for comparison, α-Bi_2O_3 (JCPDS No.41-1449) and β-Bi_2O_3 (JCPDS No.27-0050) with stoichiometric ratio were synthesized to study the influence of oxygen vacancies on the optical properties and photocatalytic performance of the prepared photocatalysts, as shown in Fig. 1(d).

The Raman spectra of all the samples were shown in Fig. 2. For α-Bi_2O_3, the characteristic Raman peak at 118 cm^{-1} was attribution to the vibration mode of Bi atoms. The peaks at 138 and 154 cm^{-1} originated to the Bi−O stretching vibration modes. The other peaks in the range of 180-500 cm^{-1} were attributed to the vibration modes of O atoms. β-Bi_2O_3 exhibited characteristic Raman peaks at 125, 313 and 465 cm^{-1}, which could be assigned to the Bi-O stretches [38,39]. For all the BiO-OVs samples, the peaks at around 140, 313, 486 and 615 cm^{-1} were assigned to BiO_{2-x}. For BiO-OVs-1 and BiO-OVs-2, the extra Raman peaks at around 550 and 520 cm^{-1} may be assigned to $Bi_2O_{2.75}$. This peak gradually disappeared as the reaction time increased due to the low content of $Bi_2O_{2.75}$. Obviously, the characteristic Raman
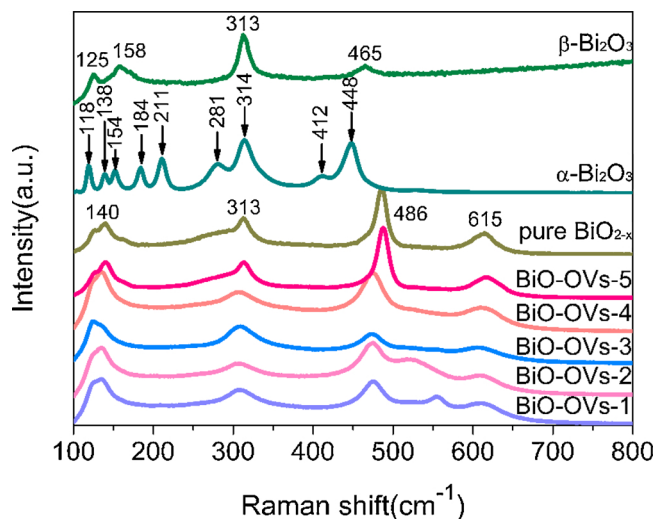

Fig. 2. Raman spectra of all samples.

peaks of BiO-OVs samples were great difference compared with α-Bi_2O_3 and β-Bi_2O_3 due to slight lattice distortion caused by the losing of oxygen atoms. The weakening and broadening of Raman peaks of BiO-OVs as well as shifted to lower frequency compared with the pure BiO_{2-x} could be ascribed to the low crystallinity, increasing concentrations of oxygen vacancies and strong interfacial interaction between $Bi_2O_{2.75}$ and BiO_{2-x} [32]. The Raman spectra further demonstrated the existence of oxygen vacancies and the formation of the heterogeneous interface.

Electron paramagnetic resonance (EPR) had been widely applied to confirm the presence of oxygen vacancies, which was an effective tool for defecting unpaired electrons in materials. As shown in Fig. 3(a), α-Bi_2O_3 and β-Bi_2O_3 exhibited no recognizable EPR signal, suggesting that there was no or low concentration of oxygen vacancies in these two samples. In contrast, BiO-OVs-2 possessed a stronger EPR signal at g value of 2.06 than that of the pure BiO_{2-x}, which meant a much higher concentration of oxygen vacancies in BiO-OVs-2. On the basis of the earlier report, the EPR signal of oxygen vacancies was usually located at g value of around 2.001 [40,41]. The increasing g value might suggest the existence of bismuth defect induced by oxygen vacancies in the as-prepared photocatalysts [42].

To ascertain the roles of oxygen vacancies in the photocatalytic processes, the optical properties of all the samples were investigated by UV–vis-NIR diffuse reflectance spectra (DRS). As shown in the inset of Fig. 3(b), α-Bi_2O_3 and β-Bi_2O_3 appeared to be pale yellow and bright yellow whereas BiO-OVs samples were in dark brown color. The change in samples' color was reflected by UV–vis-NIR DRS. Obviously, BiO-OVs and the pure BiO_{2-x} exhibited red-shifted absorption edge compared with α-Bi_2O_3 and β-Bi_2O_3 owing to the existence of oxygen vacancies. In addition, it could be seen that the absorption edges of BiO-OVs were gradually extended with the prolonging reaction time, which was
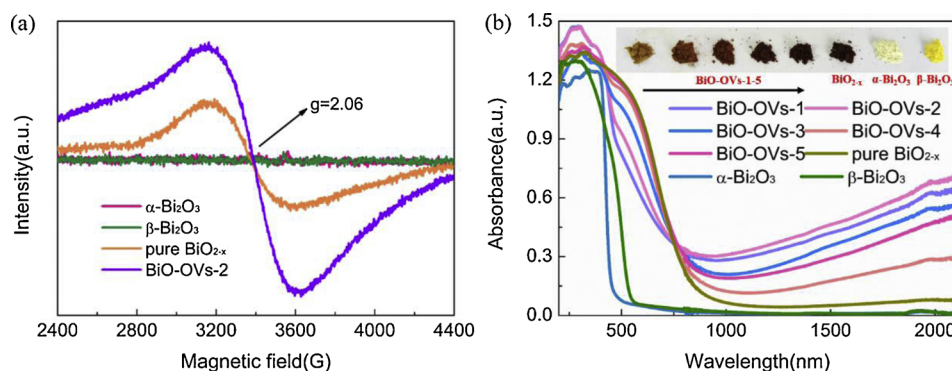
Fig. 3. (a) EPR spectra and (b) UV–vis-NIR DRS of the as-prepared samples.

consistent with the change of the colors. This phenomenon could be ascribed to the increasing content of BiO_{2-x} in the samples and the absorption edge of BiO_{2-x} was located at about 890 nm. According to the empirical formula of $E_g = 1240.8/\lambda$, the bandgap value of the pure BiO_{2-x} was calculated to be 1.39 eV. Meanwhile, a continuous and exponentially increasing absorption tail across the whole NIR range could be observed in the UV–vis-NIR DRS of all the BiO-OVs samples, which could be attributed to the localized surface plasmon resonance (LSPR) effect of oxygen vacancies. The same phenomenon was not observed in the UV–vis-NIR DRS of the pure BiO_{2-x}. Therefore, the unique LSPR effect was ascribed to the existence of oxygen vacancies in $Bi_2O_{2.75}$ instead of the oxygen vacancies in BiO_{2-x}. [43–45].

The morphological feature of as-prepared samples was characterized by the SEM and TEM images. The SEM image of BiO-OVs-2 was shown in Fig. 4(a). Obviously, the BiO-OVs-2 contained two kinds of morphology of nanosheet and irregular nanoparticle. According to the previous report, the morphology of BiO_{2-x} exhibited the nanosheet

shape [35–37]. Therefore, it could be inferred that $Bi_2O_{2.75}$ appeared to nanoparticles shape. The TEM image of BiO-OVs-2 was shown in Fig. 4(b), $Bi_2O_{2.75}$ nanoparticles tightly attached to the surface of BiO_{2-x} nanosheets with well-defined interface between BiO_{2-x} and $Bi_2O_{2.75}$, suggesting the formation of heterojunction. The HRTEM images (Fig. 4(c) and (d)) of BiO-OVs-2 further revealed the lattice fringes. The lattice fringes spacing of 3.22 Å and 2.81 Å corresponded to the (111) and (200) lattice planes of BiO_{2-x}, respectively. In addition, the lattice fringes spacing of 1.97 Å, 2.74 Å and 3.56 Å could be ascribed to the (200), (110) and (101) lattice planes of $Bi_2O_{2.75}$. The results of HRTEM images further indicated the co-existence of BiO_{2-x} and $Bi_2O_{2.75}$ and the formation of interfacial heterojunction.

The surface compositions and chemical states of α-Bi_2O_3, β-Bi_2O_3, the pure BiO_{2-x} and BiO-OVs samples were analyzed by XPS. The characteristic peaks of Bi, O and C could be identified in the XPS survey spectrum of α-Bi_2O_3, β-Bi_2O_3, the pure BiO_{2-x} and BiO-OVs-2 samples in Fig. 5(a). The C 1s peak at 284.6 eV originated from the adventitious carbon of the XPS instrument itself. The high-resolution XPS spectra of
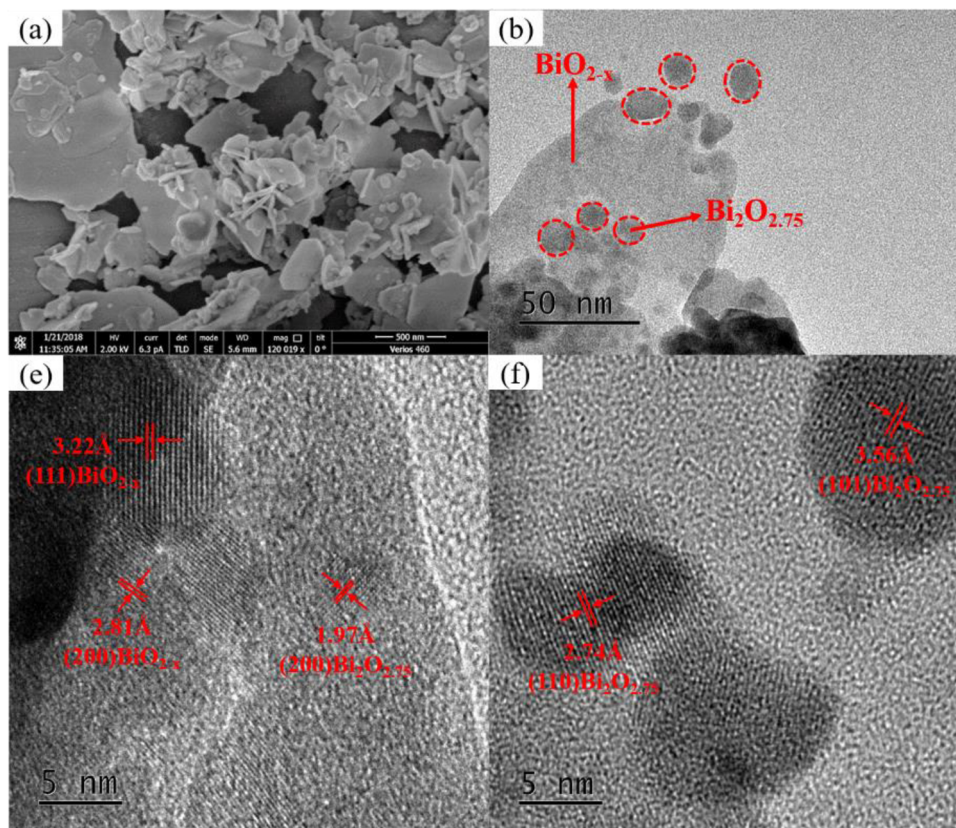

Fig. 4. (a) The SEM image of BiO-OVs-2 (b) the TEM image and (c), (d) high-resolution TEM image of BiO-OVs-2.
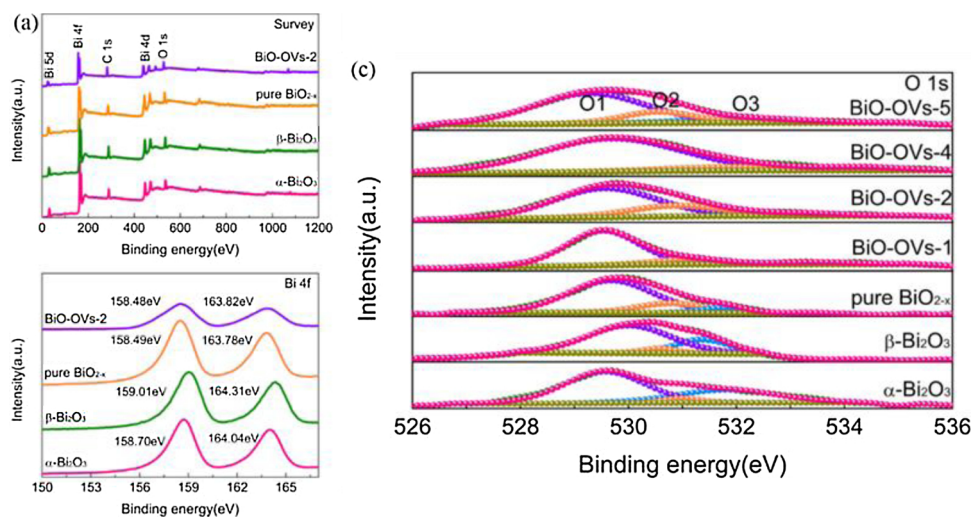
Fig. 5. XPS spectrums of α-Bi$_2$O$_3$, β-Bi$_2$O$_3$, pure BiO$_{2-x}$ and BiO-OVs-2: (a) Survey; (b) Bi 4f; (c) O 1s.

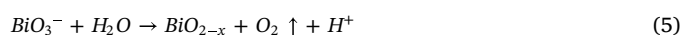**Table 1**
The binding energy and content of oxygen species.

Sample	O1		O2		O3	
	Binding energy(eV)	Content (%)	Binding energy(eV)	Content (%)	Binding energy(eV)	Content (%)
α-Bi$_2$O$_3$	529.56	62.8	530.99	4.44	531.82	32.76
β-Bi$_2$O$_3$	530.01	70.84	530.58	5.07	531.38	24.08
Pure BiO$_{2-x}$	529.68	76.03	530.78	17.52	531.78	6.44
BiO-OVs-1	529.52	82.87	531.14	11.69	533.44	5.44
BiO-OVs-2	529.55	71.19	530.88	23.84	533.13	4.97
BiO-OVs-4	529.68	87.66	531.88	8.33	534.38	4.01
BiO-OVs-5	529.28	72.77	530.55	17.26	532.18	9.97

Bi 4f was shown in Fig. 5(b). The two characteristic peaks for Bi 4f in α-Bi$_2$O$_3$, β-Bi$_2$O$_3$ located at 158.70, 164.04 and 159.01, 164.31 eV were attributed to Bi 4f$_{7/2}$ and Bi 4f$_{5/2}$, respectively. These peaks in the pure BiO$_{2-x}$ and BiO-OVs-2 shifted to lower binding energy, which could be ascribed to the formation of the Bi defect (Bi$^{(3-x)+}$, Bi^{5+}, Bi vacancy (V$_{Bi}$)) induced by oxygen vacancies [46,47], as shown in Eq. (1) and (2). Compared with the pure BiO$_{2-x}$, the XPS peaks of Bi 4f in BiO-OVs^{-2} become much wider and slightly shifted, possibly since higher concentration of oxygen vacancies and strong interfacial interaction between BiO$_{2-x}$ and Bi$_2$O$_{2.75}$ [48,49]. In Fig. 4(c), the asymmetrical O 1 s signal could be fitted into three peaks and the oxygen species of O1, O2 and O3 could be assigned to the lattice oxygen, surface oxygen vacancies or oxygen species adsorbed at oxygen vacancy sites and the surface adsorbed hydroxyl oxygen [50]. Table 1 showed the binding energy and content of three oxygen species. For α-Bi$_2$O$_3$ and β-Bi$_2$O$_3$, extremely minute amount of surface oxygen vacancies could be detected. The concentrations of surface oxygen vacancies of the pure BiO$_{2-x}$, BiO-OVs-1, BiO-OVs-2, BiO-OVs-4 and BiO-OVs-5 were calculated to be 17.52%, 11.69%, 23.84%, 8.33% and 17.26% (BiO-OVs-2 > BiO-OVs-5 > BiO-OVs-1 > BiO-OVs-4), respectively. Obviously, the concentration of surface oxygen vacancies of BiO-OVs-2 was much higher than that of α-Bi$_2$O$_3$, β-Bi$_2$O$_3$, the pure BiO$_{2-x}$, consistent with the results of EPR measurements. The enhanced light absorption of BiO-OVs samples in the NIR range could be attributed to the LSPR effect induced by surface oxygen vacancies. It could be seen from Fig. 3(b) that BiO-OVs-2 and BiO-OVs-4 exhibited the strongest and weakest light absorption in the NIR range among all BiO-OVs photocatalysts, which could be ascribed to the highest (23.84%) and lowest (8.33%) concentrations of surface oxygen vacancies of BiO-OVs-2 and BiO-OVs-4, respectively.

$$Bi^{3+} + xe^- \rightarrow Bi^{(3-x)+} \tag{1}$$

$$Bi^{3+} - 2e^- \rightarrow Bi^{5+} \tag{2}$$

The characterization results of XRD, Raman, EPR, UV–vis-NIR DRS and XPS demonstrated that the BiO$_{2-x}$/Bi$_2$O$_{2.75}$ heterojunction photocatalysts with oxygen vacancies were successfully prepared by a simple low-temperature hydrothermal method, which had attractive light absorption performance throughout the whole solar spectrum and exhibited high utilization of solar energy.

The preparation process and forming mechanism of BiO-OVs were shown in Fig. 6. Firstly, the raw material of NaBiO$_3$ was dissolved in the NaOH aqueous solution and formed Na$^+$ and BiO$_3^-$, as shown in Eq. (4). After stirring, above solution was dispersed deionized water slowly to obtain reaction precursor. Then, the reaction precursor was transferred to the PTFE autoclave and heated at 180 °C for a certain time. The BiO$_{2-x}$ nanosheets and Bi$_2$O$_{2.75}$ nanoparticles were generated during the hydrothermal reaction (Eq. (5) and (6)). At the same time, the H$^+$ generated during hydrothermal treatment. The nanoparticles of Bi$_2$O$_{2.75}$ were unstable. With the reaction time was prolonged, Bi$_2$O$_{2.75}$ nanoparticles were converted into BiO$_{2-x}$ nanosheets by dissolution-recrystallization process to obtain pure BiO$_{2-x}$ nanosheets, as shown in Eq. (7). BiO$_{2-x}$ and Bi$_2$O$_{2.75}$ were generated simultaneously in a one-step hydrothermal process. Thus, Bi$_2$O$_{2.75}$ nanoparticles were tightly attached to the surface of BiO$_{2-x}$ nanosheets with strong interfacial interaction, which was favorable to the fast interfacial migration of the photoinduced charge carriers.
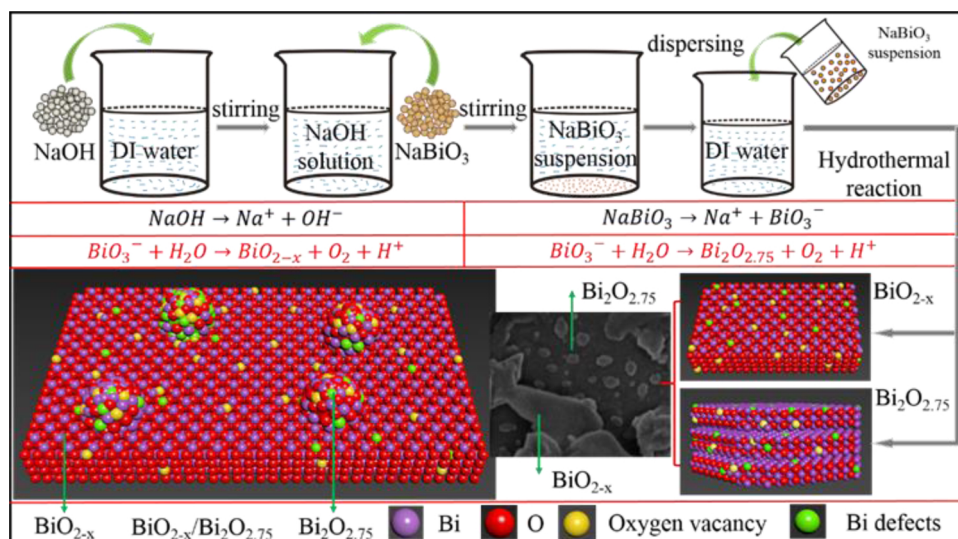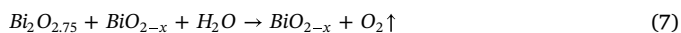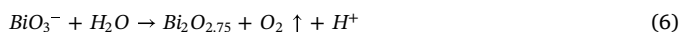
$$NaOH \rightarrow Na^+ + OH^- \tag{3}$$

$$NaBiO_3 \rightarrow Na^+ + BiO_3^- \tag{4}$$

$$BiO_3^- + H_2O \rightarrow BiO_{2-x} + O_2 \uparrow + H^+ \tag{5}$$

Fig. 6. The preparation process and forming mechanism of BiO-OVs.

$$BiO_3^- + H_2O \rightarrow Bi_2O_{2.75} + O_2 \uparrow + H^+ \tag{6}$$

$$Bi_2O_{2.75} + BiO_{2-x} + H_2O \rightarrow BiO_{2-x} + O_2 \uparrow \tag{7}$$

3.2. Theoretical calculation

In order to insight into the effects of the oxygen vacancies and the origin of full spectral response of BiO-OVs photocatalysts, the geometric and electronic structure of BiO_{2-x} and $Bi_2O_{2.75}$ with oxygen vacancies, including electron band structure and density of states, were calculated. The pristine bandgap values of BiO_{2-x} and $Bi_2O_{2.75}$ were calculated to be 2.86 eV and 1.09 eV, respectively. As shown in Fig. 7(c) and (d), the bandgap values of BiO_{2-x} and $Bi_2O_{2.75}$ reduced to 1.62 eV and 0.84 eV after the introduction of oxygen vacancies. The bandgap value obtained by theoretical calculation was slightly smaller than the experimental measurement, mainly due to the bandgap derived from DFT calculation was usually underestimated [51]. According to the earlier reports, when an interior O atom was removed from the lattice, Bi dangling bonds and two electrons were involved, which could induce abundant occupied localized energy band (defect states) located in the bottom of conduction band. These defect states could reduce the transition energy of the photoexcited electrons and result in a narrower bandgap, which was the reason of the appearance of the tail-like absorption band and

full solar spectrum absorption (consistent with the UV–vis-NIR DRS in Fig. 3(b)). The narrow bandgap indicated a high conductivity, which was beneficial to promoting the separation and the migration of the photoinduced charge carrier and improving photocatalytic activity of semiconductors [52]. The density of states of BiO_{2-x} (with oxygen vacancies) and $Bi_2O_{2.75}$ (with oxygen vacancies) were shown in Fig. 7(e), the samples of BiO_{2-x} and $Bi_2O_{2.75}$ with oxygen vacancies exhibited obviously increasing density of states at the edges of conduction bands compared with BiO_{2-x} and $Bi_2O_{2.75}$, which was related to the local lattice distortion and atom relaxation around the oxygen vacancies.

The defect structure was further calculated by first-principles density functional theory (DFT). Fig. 8(a) and (b) illustrated the optimized geometric structures of BiO_{2-x} and $Bi_2O_{2.75}$ with the incorporation of oxygen vacancies. Obviously, for BiO_{2-x}, after the introduction of an oxygen vacancy, the bond length of Bi-O near the oxygen vacancy decreased from 2.418 Å to 2.115 Å. Whereas, after the introduction of an oxygen vacancy in $Bi_2O_{2.75}$, the atoms relaxations behaviors occurred on three nearby Bi atoms. For the Bi atoms on the structure edge of $Bi_2O_{2.75}$, Bi1 (Bi2)-O bond length shortened from 2.248 Å to 2.240 Å (2.241 Å) with the lengthening of Bi (inside)-O bond from 2.511 Å to 2.529 Å. The different relaxation behavior could be ascribed to the different crystal structure between BiO_{2-x} and $Bi_2O_{2.75}$. The change of Bi-O bond length suggested that a structure distortion occurred due to
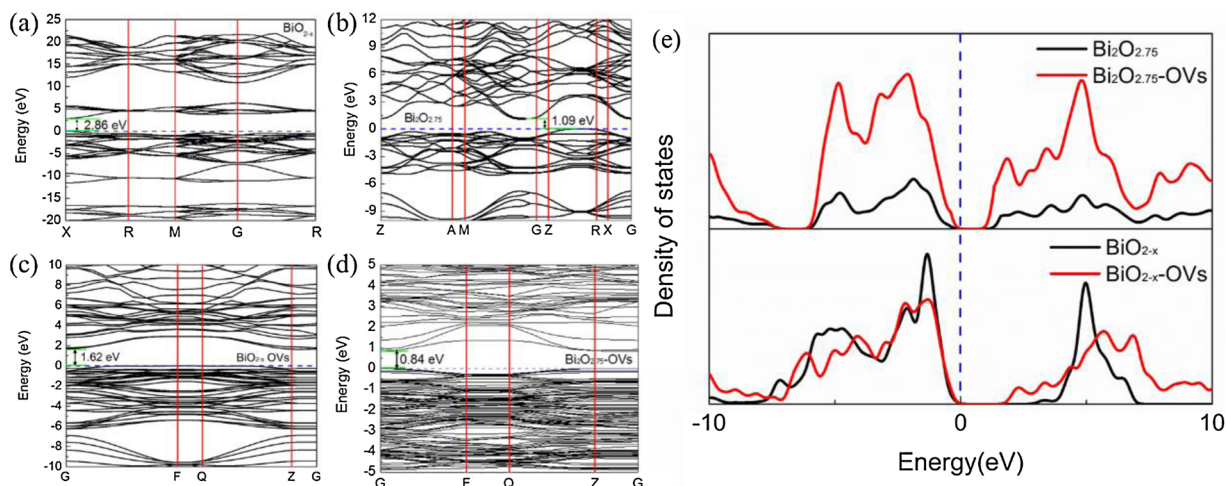

Fig. 7. The calculated electron band structures of (a) BiO_{2-x}; (b)$Bi_2O_{2.75}$; (c) BiO_{2-x} with oxygen vacancy and (d) $Bi_2O_{2.75}$ with oxygen vacancy; (e) density of states of samples.
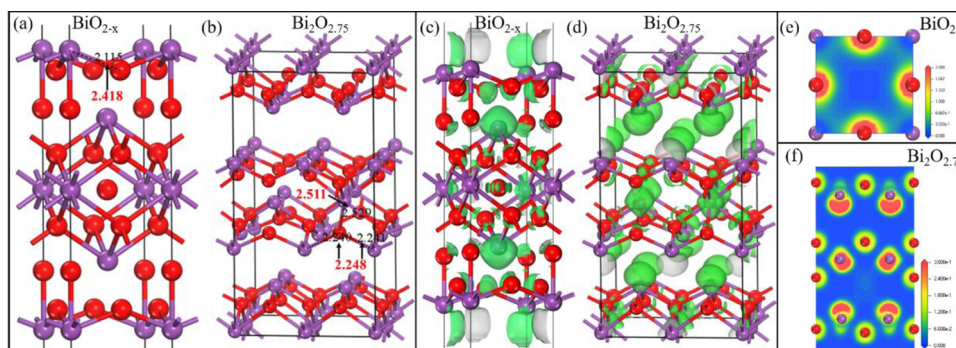
Fig. 8. Optimized geometric structures of (a) BiO_{2-x} and (b) $Bi_2O_{2.75}$ with oxygen vacancy; the corresponding 3-dimensional-simulated charge density distribution of (c) BiO_{2-x} and (d) $Bi_2O_{2.75}$ with oxygen vacancy; the 2-dimensional charge density distribution of atoms around oxygen vacancy (e)BiO_{2-x} and (f)$Bi_2O_{2.75}$.
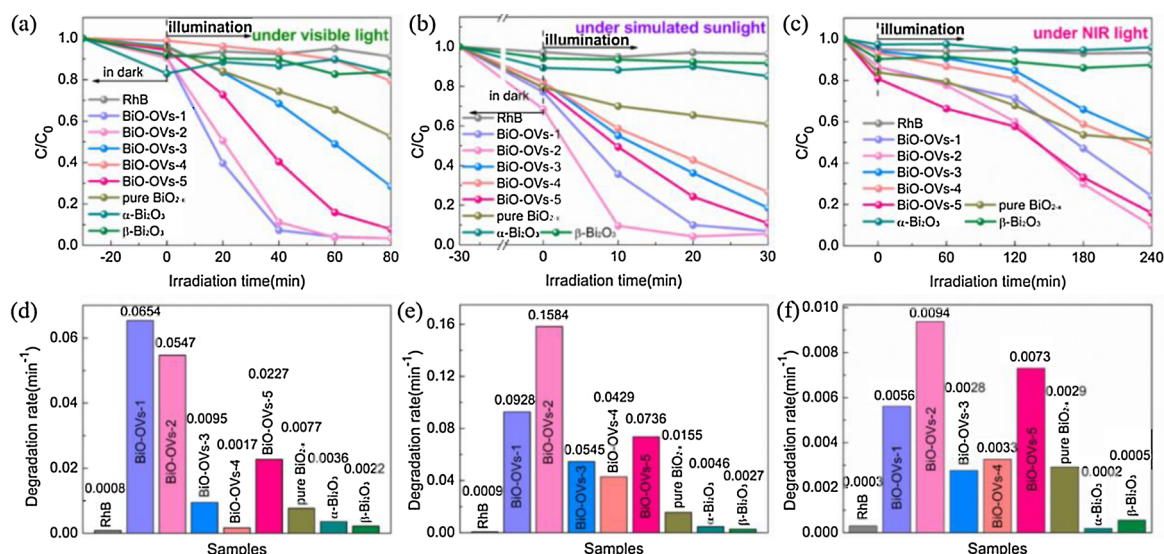

Fig. 9. The photocatalytic activities and apparent rate constants of all samples (a, d) under visible light; (b, e) under simulated sunlight;(c, f) under NIR light irradiation.

the introduction of an oxygen vacancy. The structure distortion had a significant effect on the charge density distribution of the atoms around the oxygen vacancy. The spatial charge density distribution of the atoms around the oxygen vacancy of BiO_{2-x} and $Bi_2O_{2.75}$ were shown in Fig. 8(c) and (d). Deep color represented high charge density and large contour radius represented a large charge distribution range. Obviously, the existence of oxygen vacancy resulted in the changed charge density distribution at the nearby O atoms and Bi atoms. It could be seen that the charge density of O atoms and Bi atoms around the oxygen vacancy sites was significantly higher than that of other atoms. However, the smaller range of charge density distribution could be observed, demonstrating that the existence of oxygen vacancies led to a more concentrated spatial charge distribution. The change of atom charge density would have a great effect on the energy band structure and the electron transition process. The 2-dimensional charge density distribution of BiO_{2-x} and $Bi_2O_{2.75}$ was shown in Fig. 8(e) and (f), in which red color represented the maximum charge density and blue color represented the minimum charge density as shown by the scale. As shown in Fig. 8(e), for BiO_{2-x}, the charge density of four O atoms close oxygen vacancy increased obviously. However, after the introduction of an oxygen vacancy into $Bi_2O_{2.75}$ (Fig. 8(f)), the charge density of Bi atoms and O atoms adjacent to the oxygen vacancy significantly increased. The results indicated that the introduction of oxygen vacancies in photocatalysts was favorable to redistribute charge density. Oxygen vacancies could be considered as electron acceptor. The increasing charge density would result in easier electron transition

from defect sites to conduction band and enhanced absorption and activation for O_2 molecules. The difference was that the charge distribution of BiO_{2-x} was symmetric, resulting in the overlapping centers of positive and negative charges. Inversely, the $Bi_2O_{2.75}$ had asymmetric charge distribution and separated centers of positive and negative charges, which would induce the formation of the build-in electric field. Obviously, the electrons were deprived at the Bi centers and the charge density of O atoms increased when the oxygen vacancy was introduced into $Bi_2O_{2.75}$ lattice, resulting in that the direction of the build-in electric field was from defective sites of Bi atoms to defective sites of O atoms. According to the previous reports, the VBM of Bi_2O_3 was mainly composed of O 2p orbitals with the minor contributions of Bi 6 s orbitals, whereas the CBM was mainly composed of Bi 6p orbitals [53,54]. Therefore, the existence of the build-in electric field would promote the separation of photoinduced charge carriers in the body of $Bi_2O_{2.75}$.

3.3. Photocatalytic activity

The photocatalytic performance of the as-prepared samples was evaluated by degrading RhB under visible light, simulated sunlight and NIR light irradiation. The photodegradation of RhB was used as a control experiment. It could be seen that the self-degradation efficiency of RhB without any photocatalysts was extremely low so that it could be negligible. Therefore, the removal of RhB originated to photodegradation effects of the photocatalysts. As shown in Fig. 9(a), BiO-OVs[-1] and BiO-OVs[-2] exhibited excellent photocatalytic activity under visible light

irradiation compared with other samples and nearly 93% and 89% of the RhB was degraded under 40 min of visible light irradiation. Obviously, the photocatalytic activities of BiO-OVs under simulated sunlight irradiation (Fig. 9(b)) were higher than that of under visible light irradiation due to the presence of the 4–5% ultraviolet radiation which had higher energy. Under NIR light irradiation, as shown in Fig. 9(c), BiO-OVs also exhibited high photocatalytic activity due to the enhanced light absorption in the NIR range. The light absorption characteristics of BiO-OVs photocatalysts in the NIR range depended on the concentrations of surface oxygen vacancies. Therefore, the photocatalytic performance (BiO-OVs-2 > BiO-OVs-5 > BiO-OVs-1 > BiO-OVs-4) of the prepared BiO-OVs photocatalysts under NIR light irradiation was positively correlated with its concentration of surface oxygen vacancies. Meanwhile, α-Bi_2O_3 and β-Bi_2O_3 exhibited the lower photocatalytic activity than that of the pure BiO_{2-x} and BiO-OVs heterojunction photocatalysts whether under visible light, simulated sunlight or NIR light irradiation due to narrow light absorption range and low concentrations of surface oxygen vacancies. BiO-OVs showed better photocatalytic performance than pure BiO_{2-x} which implied that heterojunction structure played an important role in improving the photocatalytic activity. The photocatalysis degradation followed the pseudo-first-order kinetics. The kinetics could be expressed as equation: $-\ln(C/C_0) = kt$, where C_0 (mg/L), C (mg/L), t (min) and k_{app} (min^{-1}) represented the initial concentration of RhB, the concentration of RhB at the irradiation time of t min, reaction time and apparent rate constant. As shown in Fig. 9(d)–(f), the apparent rate constants of BiO-OVs-2 obtaining by visible light/simulated sunlight/ NIR light irradiation were calculated to be 0.0547, 0.1584, 0.0094 min^{-1}, which were about 7.10, 10.22 and 3.24 times higher than that of the pure BiO_{2-x}. The photolysis of RhB over α-Bi_2O_3 and β-Bi_2O_3 was not observable. The above results showed that the superior photocatalytic performance of BiO-OVs could be ascribed to the synergistic effects of surface oxygen vacancies induced the LSPR effect and interfacial heterojunction.

The photocatalytic performance of the pure BiO_{2-x} and BiO-OVs photocatalysts was further evaluated by the photocatalytic NO removal under visible light irradiation to eliminate the photosensitization. As shown in Fig. S1, the pure BiO_{2-x} exhibited relatively low photocatalytic activity and 16.19% of the initial NO was removed after 12 min of visible light irradiation. Obviously, all the prepared $BiO_{2-x}/Bi_2O_{2.75}$ heterojunction photocatalysts exhibited the enhanced photocatalytic performance compared with the pure BiO_{2-x}. The removal efficiencies of NO over BiO-OVs-1, BiO-OVs-2 and BiO-OVs-3 under visible light irradiation for 12 min were calculated to be 55.85%, 55.71% and 57.67%, which were 3.45, 3.44 and 3.56 times higher than that of the pure BiO_{2-x}, respectively. The results further demonstrated that the enhanced photocatalytic activity of BiO-OVs photocatalysts was attributed to the promoting photoinduced charge carriers' separation due to the formation of the interface heterojunction between BiO_{2-x} and $Bi_2O_{2.75}$.

It could be seen that BiO-OVs photocatalysts exhibited a relatively low light absorption intensity in the range of 700–1200 nm in the UV–vis–NIR DRS. In order to further investigate the full solar spectrum responsive characteristics of BiO-OVs photocatalysts and the role of the LSPR effect of oxygen vacancies, the photo-degradation experiments of RhB over BiO-OVs-2 were carried out under monochromatic LED light irradiation (740 nm, 850 nm, 940 nm and 1100 nm). As shown in Fig. 10(a), the BiO-OVs-2 exhibited excellent photocatalytic performance under the illumination of long light wavelengths. The phenomenon might be ascribed to the LSPR effect of surface oxygen vacancies, which had been confirmed by UV–vis–NIR DRS spectra. Moreover, the degradation rates of RhB over BiO-OVs-2 were calculated to be 0.01158, 0.00823, 0.00614 and 0.00866 min^{-1} under 740, 850, 940 and 1100 nm light irradiation, respectively. In the range of NIR light, when the wavelength of monochromatic light was 1100 nm, BiO-OVs-2 showed the highest apparent rate constant. Based on the above results, the as-prepared BiO-OVs photocatalysts with oxygen vacancies

possessed superior light photocatalytic activity throughout the whole solar spectrum.

The stability of photocatalysts was critical to its practical application. Therefore, the stability of BiO-OVs-2 was studied by recycling the photocatalyst for the photo-degradation of RhB under visible light irradiation. Based on the Fig. S2(a), it could be noticed that the photocatalytic activity of BiO-OVs-2 photocatalyst did not apparently deactivate after six times cycle, indicating that the BiO-OVs photocatalysts as-prepared in this work had excellent stability and degradation activity for the removal of RhB. Furthermore, the XRD pattern of BiO-OVs-2 after 6th run cycle was shown in Fig. S2(b). The XRD patterns of BiO-OVs-2 before and after the cycle tests were unchanged, indicating that the phase structure of photocatalyst had not been destroyed. The above results showed that the as-prepared BiO-OVs photocatalysts had good stability. The absorbance curves of RhB were showed in Fig. S2(c). Compared with the first photo-degradation reaction, as the number of cycles increased, the characteristic absorption peak of RhB appeared to be obvious blue shift, which could be attributed to the reaction of step-by-step de-ethylated in the photocatalytic process [55,56]. The phenomenon was mainly caused by the decreased redox ability of the BiO-OVs-2 photocatalyst, which could be ascribed to the refilling of oxygen vacancies by seizing the oxygen atoms from adsorbed hydroxyl oxygen or oxygen molecules. This conjecture could be proven by XPS test. As shown in Fig. S3(a), the XPS survey did not significantly change, consisting with XRD result. The concentration of oxygen vacancies reduced from 23.84% to 17.66% after the cycle reaction (Fig. S3(b)), which further demonstrated that the oxygen vacancies could be filled during the photocatalytic process.

To investigate the universal application of the prepared BiO-OVs photocatalysts, the photocatalytic activity of BiO-OVs was further evaluated by the degradation of methyl orange (MO) and acid red (AR) aqueous solutions under visible and NIR light irradiation. As everyone known, RhB was cationic dye and MO and AR were anionic dyes inversely [57–59]. As shown in Fig. S4(a) and (b), after visible light irradiation for 60 min and 40 min, MO and AR almost completely degraded over BiO-OVs-2. Likewise, after NIR light irradiation for 150 min, the degradation rates of MO and AR over BiO-OVs-2 were about 76.9% and 88.5% (Fig. S4(c) and (d)), respectively. The above results indicated that the as-prepared BiO-OVs photocatalysts was not selective in the degradation of organic dyes and had a high practical application value.

3.4. Photocatalytic mechanism

Generally, the photocatalytic process involved a series of surface redox reactions of photoinduced electrons and holes, which may react with adsorbed O_2 and H_2O and produce reactive oxygen species, such as superoxide radical ($\cdot O_2^-$) and hydroxyl radical ($\cdot OH$) to further react with RhB molecules. Reactive species trapping experiments were employed to investigate the role of individual reactive species and clearly understand the photocatalytic mechanism in degradation process. Different reactive species scavengers, including benzoquinone (BQ, a $\cdot O_2^-$ scavenger), sodiumoxalate ($Na_2C_2O_4$, a h^+ scavenger) and Tert-butyl alcohol (tBuOH, a $\cdot OH$ scavenger) were added into the photocatalytic system (the BiO-OVs-2 was used as photocatalyst), respectively [35,60,61]. As shown in Fig. S5(a), under visible light irradiation, the degradation of RhB was significantly inhibited when tBuOH and BQ were added, demonstrating that $\cdot OH$ radical was the most critical reactive species and $\cdot O_2^-$ radical was considered as a secondary reactive species in the whole photocatalytic reactions. However, when $Na_2C_2O_4$ was added, the degradation rate of RhB slightly decreased, which suggested that h^+ was not the main reactive species for RhB degradation. Under NIR light irradiation, as shown in Fig. S5(b), the degradation efficiency of RhB solution decreased from 90.3% to 8.2% and 16.6% after the introduction of the BQ and tBuOH, suggesting $\cdot O_2^-$ and $\cdot OH$ radicals played crucial role in the degradation by BiO-OVs-2.
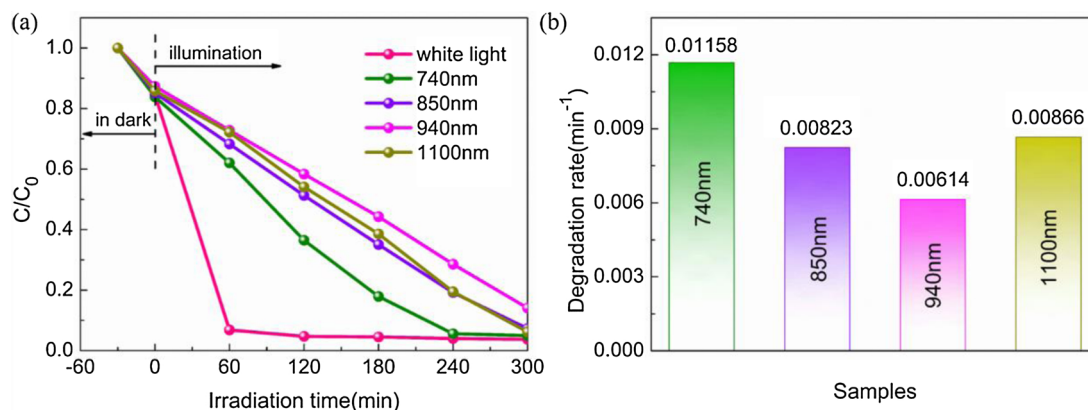
Fig. 10. (a) Photocatalytic activities of BiO-OVs-2 for the degradation of RhB under monochromatic visible light (740 nm) and NIR light (850, 940 and 1100 nm) irradiation; (b) the corresponding apparent rate constants.

Whereas, the introduction of $Na_2C_2O_4$ only slightly reduced the degradation efficiency of RhB over BiO-OVs-2. This result indicated the contribution of all the active species ($\cdot OH > \cdot O_2^- > h^+$) to the RhB degradation.

The EPR technique with DMPO (5, 5-dimethyl-1-dimethy-*N*-oxide) as a radical scavenger was carried out to further elucidate the generation of reactive oxygen species and photocatalytic degradation mechanism. The EPR signals of BiO-OVs-2 with DMPO in methanol solution (for DMPO-$\cdot O_2^-$) or aqueous solution (for DMPO-$\cdot OH$) were measured under visible/NIR light irradiation at room temperature and air atmosphere. As shown in Fig. 11(a)–(d), obvious EPR signals of $\cdot O_2^-$ and $\cdot OH$ were observed under dark conditions, which could be attributable to the improved absorption and activation ability for O_2

molecules due to the presence of abundant localized electrons at oxygen vacancy sites. The free electrons trapped by oxygen vacancies could react with O_2 molecules to generate $\cdot O_2^-$ radical ($O_2 + e^- \rightarrow \cdot O_2^-$). Moreover, the generated $\cdot O_2^-$ radical could react with H^+ and electrons to produce H_2O_2 ($\cdot O_2^- + 2H^+ + e^- \rightarrow H_2O_2$) or O_2 directly reacted with two electrons and two H^+ to generate H_2O_2 ($O_2 + 2e^- + 2H^+ \rightarrow H_2O_2$). H_2O_2 molecules further dissociated to form $\cdot OH$ radical ($H_2O_2 + e^- \rightarrow \cdot OH + OH^-$) [62]. Therefore, the EPR signals of $\cdot O_2^-$ and $\cdot OH$ radicals could be detected in dark. In order to confirm the enhanced activation capacity for O_2 molecules of BiO-OVs-2, the EPR tests of BiO-OVs-2 and BiO_{2-x} at different time in dark were carried out, as shown in Fig. S6. The obvious EPR signals of $\cdot O_2$–DMPO could be detected over BiO-OVs-2 photocatalyst after 5, 10, 15 min of dark
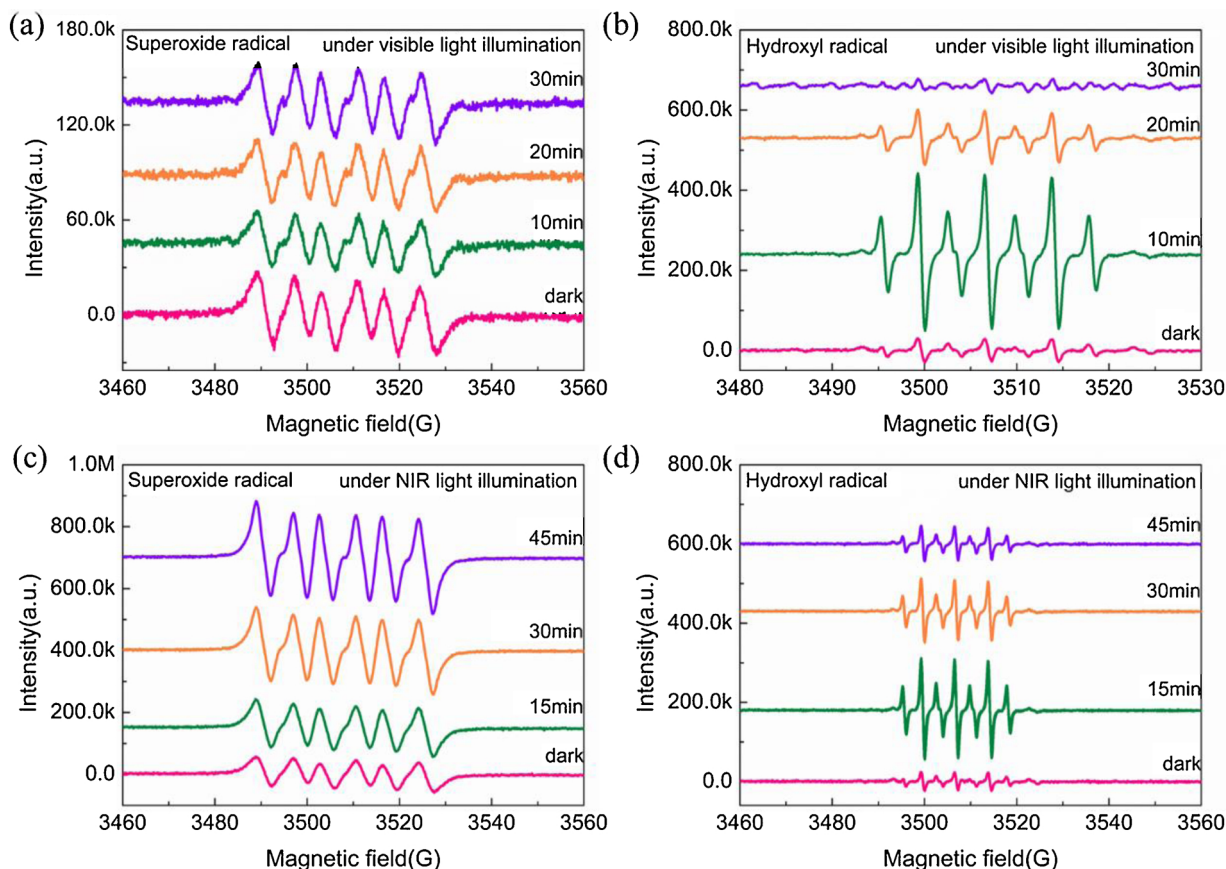

Fig. 11. EPR signals of the (a) DMPO-$\cdot O_2^-$ and (b) DMPO-$\bullet OH$ under visible light irradiation; (c) DMPO-$\cdot O_2^-$ and (d) DMPO-$\cdot OH$ under NIR light irradiation of BiO-OVs-2.

reaction. For the pure BiO_{2-x}, the similar phenomenon has not been observed, demonstrating that BiO-OVs-2 exhibited enhanced activation capacity for O_2 molecules than that of the pure BiO_{2-x}. The stronger activation capacity for O_2 of BiO-OVs-2 could be ascribed to the existence of higher concentration of surface oxygen vacancies with abundant localized electrons. Based on the above analysis, the decreasing concentration of dye solution (Figs. 9, Fig. S2 and Fig. S4) during dark reaction could be attributed to the synergistic effect between surface absorption and degradation reaction. Surface oxygen vacancies played a positive role in promoting the formation of $·O_2^-$ radical and the dissociation of H_2O_2 molecules in dark [63]. After visible/NIR light irradiation, the six stronger characteristic peaks of the DMPO-$·O_2^-$ adducts were observed over BiO-OVs-2, which suggested a higher concentration of $·O_2^-$ radical was produced by the reduction reaction between photoinduced electrons and O_2 molecules [64,65]. In addition, seven strong characteristic peaks with intensity of 1:2:1:2:1:2:1 were generated by BiO-OVs-2, which represented the appearance of DMPOX due to the oxidation of DMPO by two $·OH$, demonstrating the generation of $·OH$ radical by the oxidation reaction between adsorbed H_2O and photoinduced holes [66]. With the irradiation time prolonged, the intensity of characteristic EPR signals of DMPOX gradually reduced, which could be attributed to the consumption of DMPO during the reactions. The EPR results further indicated that $·OH$ and $·O_2^-$ species played a significant role in the photocatalytic process, which were consistent with the results of trapping experiments. In order to research the source of $·O_2^-$ radical, the photocatalytic performance of BiO-OVs-2 was evaluated by the photodegradation of RhB under LED white light irradiation under vacuum conditions, as shown in Fig. S7. Interestingly, BiO-OVs-2 exhibited enhanced photocatalytic activity under vacuum conditions, demonstrating that $·O_2^-$ radical was mainly derived from absorbed oxygen at oxygen vacancy sites rather than dissolved oxygen during photocatalytic reactions. Moreover, under vacuum conditions, bulk oxygen vacancies tended to migrate to the surface, resulting in the increasing concentration of surface oxygen vacancies. Compared with the initial photocatalytic system, the increased concentration of surface oxygen vacancies could improve the separation efficiency of photoinduced electron-hole pairs and the adsorption and activation ability of H_2O molecules, resulting in the enhanced photocatalytic performance under vacuum conditions.

The photoelectrochemical performance of BiO-OVs and pure BiO_{2-x} were investigated by transient photocurrent response, EIS Nyquist and Mott-Schottky plots. The transient photocurrent response was widely used to study the generation of the photoinduced charge carriers and the interfacial transfer process. The transient photocurrent value could directly reflect the separation efficiency and the migration rate of the photoinduced charge carriers [67,68]. Fig. 12(a) showed the transient photocurrent response of BiO-OVs and the pure BiO_{2-x} over several on-off cycles under visible light irradiation without applied bias. Obviously, all the samples exhibited quick and reproducible photocurrent response. BiO-OVs-1 possessed the highest photocurrent value, which was about 6.72 time higher than that of the pure BiO_{2-x}. As shown in Fig. 12(b), with the increasing of the applied bias, the excellent photocurrent response of BiO-OVs had not significantly change. The results indicated that the as-prepared BiO-OVs photocatalysts had great separation ability of photoinduced electron-hole pairs. Moreover, electrochemical impedance spectroscopy (EIS) were conducted to further investigate the photogenerated charge carriers' generation and migration process of BiO-OVs and the pure BiO_{2-x}. On the basis of Fig. 12(c), EIS Nyquist plot of BiO-OVs exhibited much smaller arc radius except BiO-OVs-4 than that of the pure BiO_{2-x}, indicating lower charge carrier transfer resistance of $BiO_{2-x}/Bi_2O_{2.75}$ heterojunction photocatalysts due to the suppressed recombination of the photogenerated electrons and holes [69]. The larger arc radius of BiO-OVs-4 compared with other samples could be ascribed to the lower concentration of oxygen vacancies, which played an important role in promoting the separation

and migration of the photogenerated charge carriers. The EIS Nyquist plots of BiO-OVs and the pure BiO_{2-x} could be fitted by the ZsimpWin software. The used circuit model was $R_s(CR_{ct}(QR_a))$, where R_s, C, R_{ct}, Q and R_a represented solution resistance, space change capacitance, charge transfer resistance, electrochemical double-layer capacitance and electrolytic resistance, respectively. The fitting data were listed in Table 2. It could be seen that the R_{ct} values of BiO-OVs and pure BiO_{2-x} were 34.49, 148.7, 436.6, 1109, 243.9 kΩ under visible light irradiation, respectively. BiO-OVs exhibited the smallest charge transfer resistance, which was consistent with the result of the transient photocurrent response. The small charge transfer resistance was beneficial to generating more electrons and holes to participate in photocatalytic reactions. Mott-Schottky (MS) experiments in dark were conducted to explore the intrinsic electronic properties of the prepared photocatalysts. As shown in Fig. 12(d), both BiO-OVs samples and the pure BiO_{2-x} exhibited the characteristics of n-type semiconductor [70]. According to the formula (8) and (9), the slope of linear part of MS curve was negatively correlated with carrier concentration [71]. Obviously, BiO-OVs had the smallest slope, suggesting the highest donor density owing to the existence of high concentration of oxygen vacancies. Therefore, the excellent photocatalytic activity of BiO-OVs could be ascribed to the extremely high efficiency of defect-mediated separation and migration of the photoinduced charge carriers. According to the intercept between the linear part and the X-axis, the CB potential of pure BiO_{2-x} was calculated to be -0.53 V, approximately. According to the calculation results of the energy band structure, the VB potential of pure BiO_{2-x} was 2.33 V.

$$\frac{1}{C^2} = \frac{2}{e\varepsilon\varepsilon_0 N_D}\left(E - E_{fb} - \frac{kT}{e}\right) \tag{8}$$

$$N_D = \frac{2}{e\varepsilon\varepsilon_0}[\frac{d(\frac{1}{c^2})}{d(E)}]^{-1} \tag{9}$$

The CB and VB position of $Bi_2O_{2.75}$ could be estimated by the follow Eqs. (10) and (11):

$$E_{CB} = X - E^\theta - 0.5E_g \tag{10}$$

$$E_{VB} = E_V + E_g \tag{11}$$

Where E_{CB} was conduction band edge, E_{VB} represented valence band edge, X was the absolute electronegatively of the semiconductors, expressed as the geometric mean of the absolute electronegativity of the constituent atoms and E^θ represented the energy of free electron on the hydrogen scale (about 4.5 eV) [72]. The Mulliken electronegativity of Bi and O were 4.69 and 7.54, respectively. The X value of $Bi_2O_{2.75}$ was calculated to be 6.17, approximately. Therefore, the CB and VB edges of $Bi_2O_{2.75}$ were calculated to 1.13 eV and 2.22 eV, respectively.

On the basis of the above-mentioned band energy level analysis, active species trapping experiments and EPR measurements, a novel defect-induced Z-scheme mechanism for enhanced full solar spectrum-driven photocatalytic activity of $BiO_{2-x}/Bi_2O_{2.75}$ heterojunction photocatalyst was proposed. Due to the narrow bandgaps, under visible light irradiation, both BiO_{2-x} and $Bi_2O_{2.75}$ could be excited to generate photoinduced electron-hole pairs. The active species trapping experiments and EPR measurements demonstrated the generation of $·O_2^-$ and $·OH$ radicals under visible light irradiation. If $BiO_{2-x}/Bi_2O_{2.75}$ composites followed the conventional I-type heterojunction, as shown in Fig. 13, the photoinduced electrons (holes) tend to transfer from the CB (VB) of BiO_{2-x} to the CB (VB) of $Bi_2O_{2.75}$. However, the CB potential of $Bi_2O_{2.75}$ was more positive (+1.13 eV vs. NHE) than the standard redox potential of $·O_2^-/O_2$ (-0.33 eV vs. NHE) [73] and $·O_2^-$ radical cannot generate at this condition. For the above reason, a possible Z-scheme heterojunction was proposed and the charge transfer pathways was showed in Fig. 14. For $Bi_2O_{2.75}$, the VBM and CBM was mainly composed of O 2p and Bi 6p orbitals, respectively. Due to the presence of build-in electric field from Bi defect sites to O defects induced by
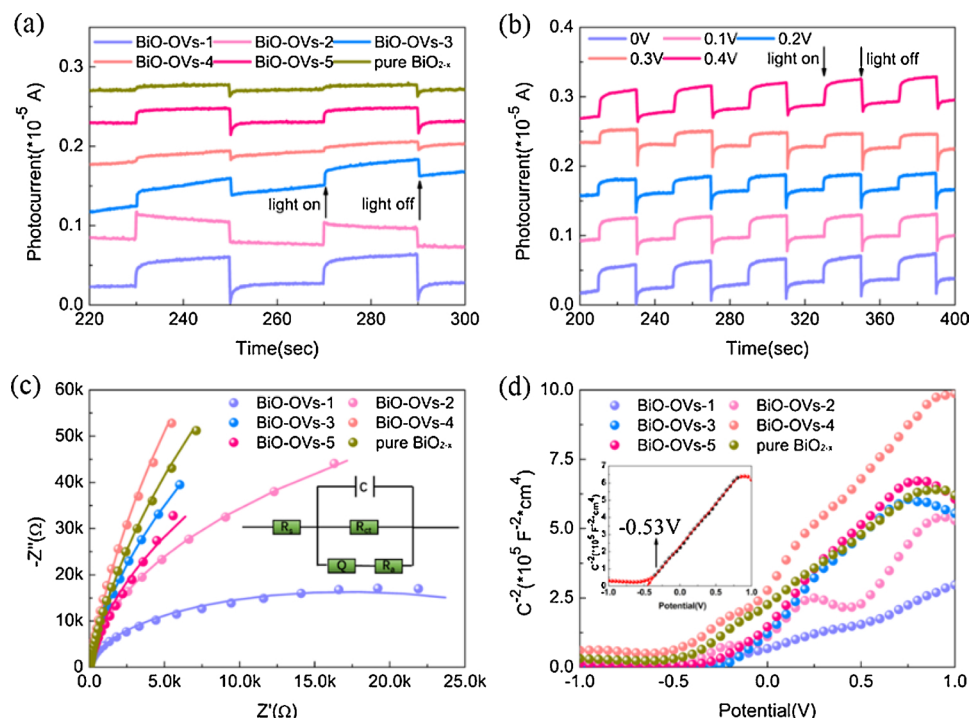
Fig. 12. The transient photocurrent response (a) without applied bias and (b) with different applied bias; (c) EIS Nyquist plots and Mott-Schottky plots of all samples.

Table 2
Z-fit equivalent circuit date of samples.

Sample	$R_s(\Omega)$	$C(\times 10^{-8} F)$	$R_{ct}(\times 10^4 \Omega)$	$Q(\times 10^{-5} Ssec^n)$	n	$R_a(\Omega)$
BiO-OVs-1	8.261	9.467	3.449	2.991	0.9658	26.84
BiO-OVs-2	12.97	10.38	14.86	3.062	0.9755	26.99
BiO-OVs-3	9.223	8.648	43.66	3.889	0.9621	27.56
BiO-OVs-4	7.195	8.993	110.9	2.907	0.9676	25.55
BiO-OVs-5	7.02	8.036	24.39	4.622	0.9643	27.06
Pure BiO_{2-x}	6.609	7.276	73.39	2.98	0.9604	28.94

Fig. 14. Proposed photocatalytic mechanism over Z-scheme $BiO_{2-x}/Bi_2O_{2.75}$ heterojunction photocatalyst.
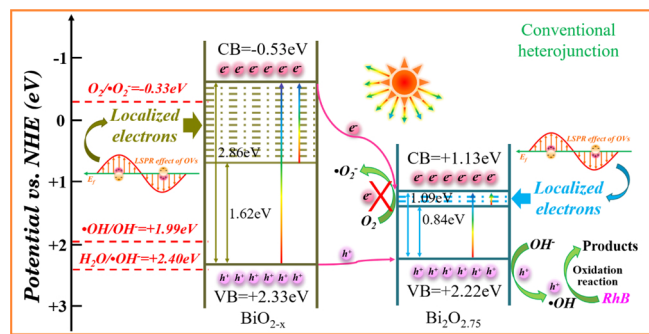

Fig. 13. The photocatalytic mechanism of conventional Type I heterojunction.

asymmetric charge distribution, it is difficult that the photoinduced electrons at CB position recombined with the photoinduced holes at VB position. Therefore, contrast to conventional I-type heterojunction mechanism, photoinduced electrons of $Bi_2O_{2.75}$ would recombine with the photoinduced holes of BiO_{2-x} and photoinduced electrons of BiO_{2-x} with strong reduction ability could be retained. The CB potential (-0.53 eV vs. NHE) of BiO_{2-x} was more negative than the redox potential of $\cdot O_2^-/O_2$ and $\cdot O_2^-$ radical could be produced by the reduction reaction between O_2 molecules and the CB electrons of BiO_{2-x}. The VB potential of $Bi_2O_{2.75}$ was positive enough and the VB holes of $Bi_2O_{2.75}$ could react with OH^- to generate $\cdot OH$ radical.
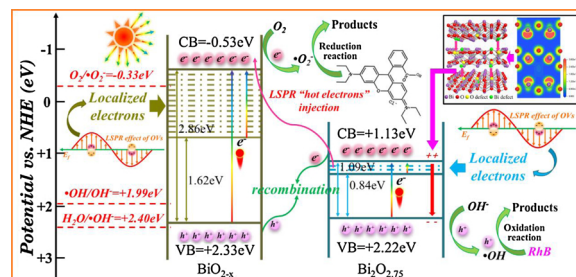
Under NIR light irradiation, $\cdot O_2^-$ and $\cdot OH$ radicals also played an important role for the photo-degradation of RhB. However, the reaction mechanism was different. Under long wavelength light irradiation, the free electrons located at oxygen vacancy sites of BiO_{2-x} and $Bi_2O_{2.75}$ would instantaneously reach a high-energy SP state to generate plasmonic "hot electrons". The "hot electrons" would be injected into the CB of BiO_{2-x} and $Bi_2O_{2.75}$ to increase electron density and enhance photocatalytic performance. Interestingly, partial high-energy LSPR "hot electrons" of $Bi_2O_{2.75}$ could be injected into the CB of BiO_{2-x} with more negative CB potential and reacted with O_2 to generate $\cdot O_2^-$ radicals, resulting in high photocatalytic activity. This mechanism was further proved by EPR measurements of DMPO-$\cdot O_2^-$ under NIR light irradiation, as shown in Fig. S8. For pure BiO_{2-x}, only free electrons trapped by oxygen vacancies could be excited to CB to participate in photocatalytic reactions. Therefore, the extremely weak EPR signals of DMPO-$\cdot O_2^-$ could be obtained under NIR light irradiation for pure BiO_{2-x}. Obviously, the characteristic signal peaks of DMPO-$\cdot O_2^-$ of $BiO_{2-x}/Bi_2O_{2.75}$ were stronger than that of the pure BiO_{2-x} whether in dark or under NIR light irradiation. $Bi_2O_{2.75}$ could be excited by NIR light to generate photoinduced electron-hole pairs and high-energy "hot electrons" due to small bandgap energy and the LSPR effect of oxygen vacancies. However, the CB potential of $Bi_2O_{2.75}$ was more positive than that of $O_2/\cdot O_2^-$ and $\cdot O_2^-$ radical could not be generated by the reaction between the CB electrons of $Bi_2O_{2.75}$ and O_2. Therefore, the LSPR "hot
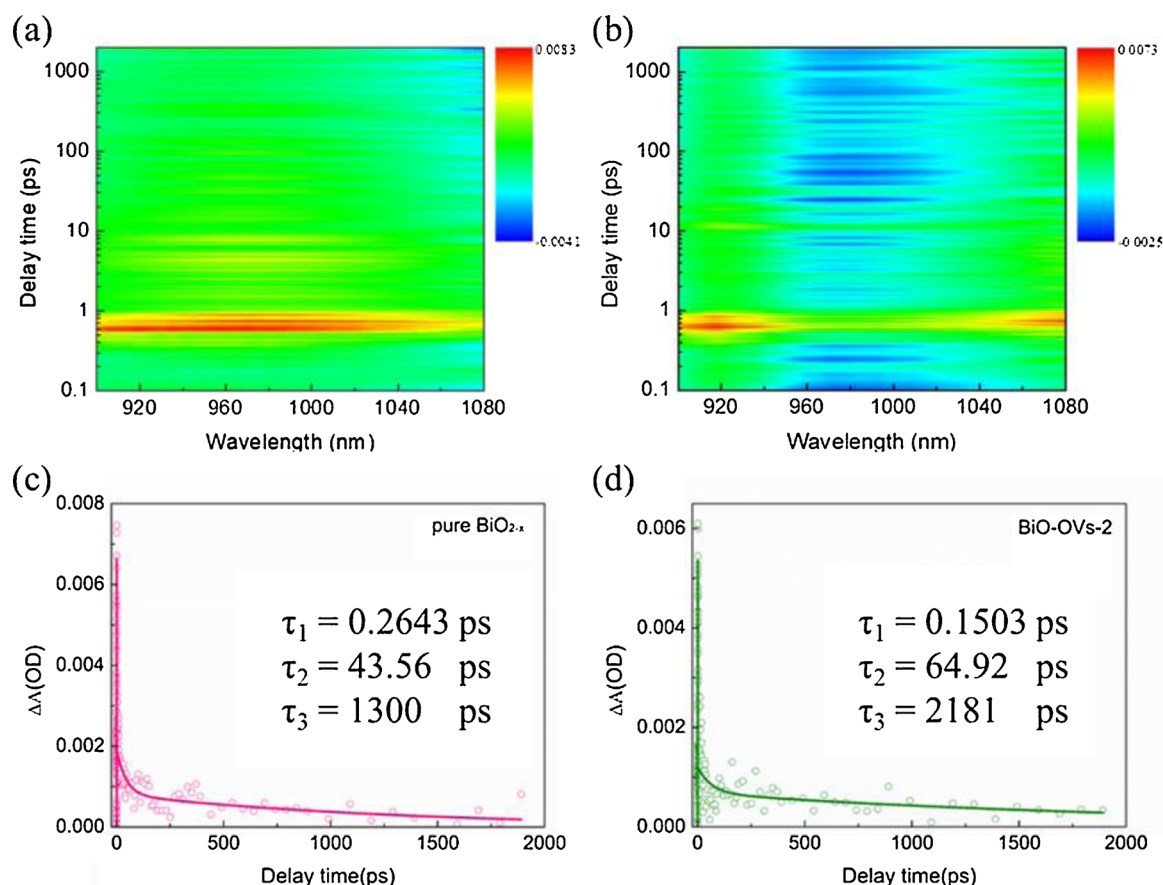
Fig. 15. The ultrafast transient spectra of (a) the pure of BiO_{2-x} and (b) BiO-OVs-2; Normalized transient absorption traces observed at 920 nm of (a) the pure BiO_{2-x} and (b) BiO-OVs-2 (bold lines indicated multi-exponential curves fitted to kinetic traces).

electrons" with high energy of $Bi_2O_{2.75}$ would be injected into the CB of BiO_{2-x} with more negative potential and react with O_2 to generate more $\cdot O_2$- radicals. These reactive species of $\cdot O_2$-, $\cdot OH$ and h^+ further reacted with RhB to form CO_2, H_2O and other inorganic molecules. Based on the above analysis, highly active $BiO_{2-x}/Bi_2O_{2.75}$ photocatalysts with full solar spectrum-driven could be attributed to the synergistic effect between oxygen vacancies with the LSPR effect and the Z-scheme heterogeneous interface between BiO_{2-x} and $Bi_2O_{2.75}$.

In order to further verify the defect-induced Z-scheme mechanism of $BiO_{2-x}/Bi_2O_{2.75}$ heterojunction photocatalyst, the femtosecond time-resolved transient absorption (fs-TA) spectral was carried out. The ultrafast transient absorption spectral of the pure BiO_{2-x} and BiO-OVs-2 were shown in Fig. 15(a) and (b). Overall, the intensity of stimulated radiation of BiO-OVs-2 heterojunction photocatalyst was lower than that of the pure of BiO_{2-x}, suggesting a rapid electrons transfer process at the interface between BiO_{2-x} and $Bi_2O_{2.75}$. This phenomenon indicated that the formation of interfacial heterojunction was favorable to the separation and migration of photoinduced charge carriers. In the range of 950–1040 nm, with the prolonged time of pulse laser excitation, the decreasing intensity of BiO-OVs-2 was attributed to the accelerated radiation decay kinetics [74]. Fig. 15(c) and (d) exhibited the normalized transient absorption traces up to 1.9 ns of the pure BiO_{2-x} and BiO-OVs-2 at 920 nm to further evaluate the decay kinetics of the photoinduced electron-hole pairs. The time profiles were fitted using a three-exponential function with the lifetimes 0.2643 (τ_1), 43.56 (τ_2) and 1300 ps (τ_3) for the pure BiO_{2-x}, while those were 0.1503 (τ_1), 64.92 (τ_2) and 2180 ps (τ_3) for BiO-OVs-2. Generally, τ_1, τ_2 and τ_3 were assigned for the $e^-_{trapped}$ on the trapping site, the diffusion of $e^-_{trapped}$ to the oxygen vacancies sites and the diffusion of $e^-_{trapped}$ to the reaction sites for the photocatalytic reaction such as the oxygen reduction

($O_2 + e^-_{trapped} \rightarrow O_2^-$), respectively [75]. The values of τ_2 and τ_3 of BiO-OVs-2 were much higher than that of the pure BiO_{2-x} due to the higher concentration of surface oxygen vacancies, which could provide more active sites for photocatalytic reaction. Therefore, BiO-OVs-2 exhibited enhanced photocatalytic activity than that of the pure BiO_{2-x} owing to the longer lifetime of photoinduced electrons and holes.

The high redox ability of Z-scheme $BiO_{2-x}/Bi_2O_{2.75}$ heterojunction photocatalysts was demonstrated by linear sweep voltammetry (LSV) and cyclic voltammetry (CV) curves. As could be seen from Fig. 16(a), the BiO-OVs exhibited the increased photocurrent density compared to the pure BiO_{2-x}, which was consistent with the transient photocurrent results. The strong oxidation peaks in all LSV curves between -0.6 V and $+0.6$ V could be attributed to the Faradaic reaction: $BiO_{2-x}/Bi_2O_{2.75} + H_2O + e^- \rightarrow Bi + OH^-$ [76]. Moreover, another obvious oxidation peak around 1.4 V was ascribed to the oxygen evolution reaction [77]. Obviously, BiO-OVs photocatalysts exhibited stronger oxidation peak than that of the pure BiO_{2-x}, demonstrating stronger oxidation ability. The CV curves of BiO-OVs and pure BiO_{2-x} were shown in Fig. 16(b). A couple of well-defined characteristic redox peaks was observed between -0.6 and 1.5 V, which were consistent of the LSV curves. The shift of the peaks could be ascribed to the different concentrations of oxygen vacancies. Remarkably, the area integration of BiO-OVs within the CV curve was larger than that of the pure BiO_{2-x}, indicating that the as-prepared heterojunction photocatalysts possessed higher redox ability [78]. The mineralization ability of Z-scheme $BiO_{2-x}/Bi_2O_{2.75}$ photocatalysts is further verified by TOC measurement. As shown in Fig. 17(a), the TOC removal rate of the pure BiO_{2-x} and BiO-OVs-2 reached about 42.14% and 64.33% under 120 min of visible light irradiation, respectively. This result indicated the better photocatalytic mineralization of $BiO_{2-x}/Bi_2O_{2.75}$ for RhB. Moreover, the TOC removal
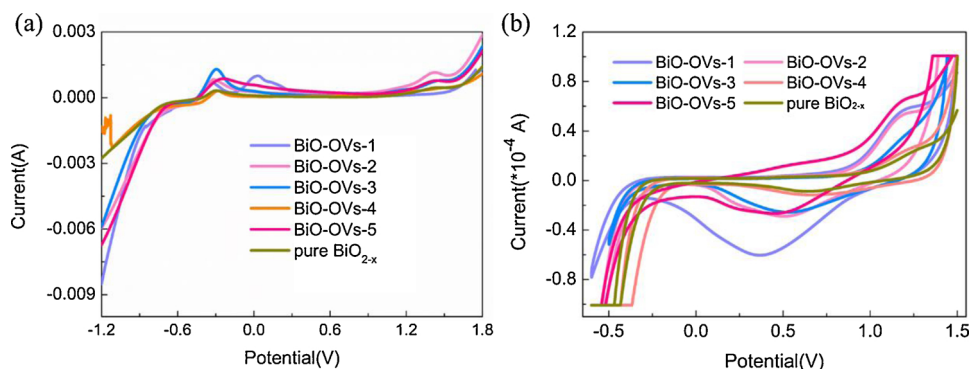
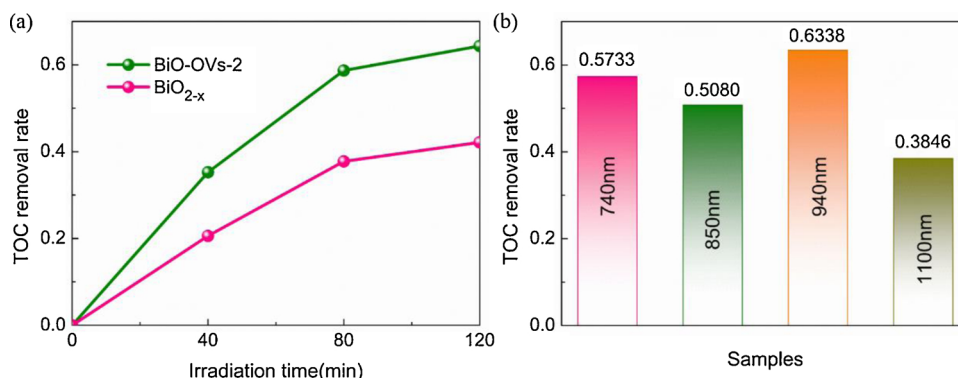**Fig. 16.** (a) LSV and (b) CV curves of the as-prepared samples.

Fig. 17. The TOC removal rate of RhB over (a) the pure BiO_{2-x} and BiO-OVs-2 under visible light irradiation; (b) BiO-OVs-2 under monochromatic light irradiation (C_0 - 20 mg/L, BiO_{2-x}/BiO-OVs-2 - 2 g/L).
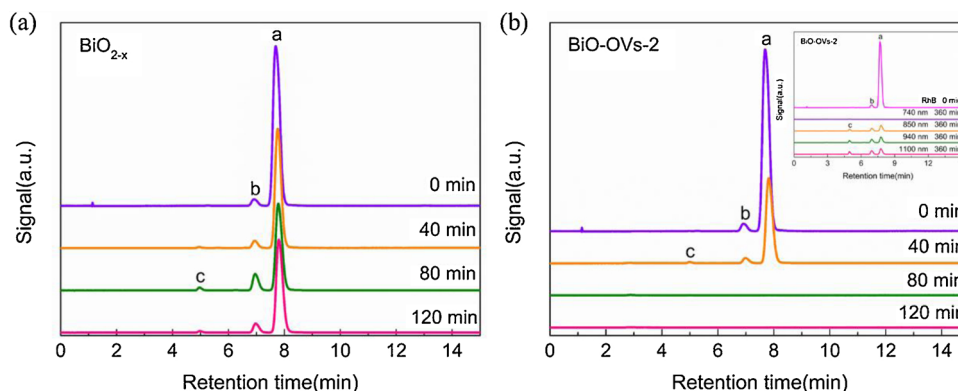

Fig. 18. The HPLC chromatograms of RhB photodegradation over (a) the pure BiO2-x and (b) BiO-OVs-2 under visible light irradiation.

rates of RhB over BiO-OVs-2 was calculated to be 57.33%, 50.80%, 63.38% and 38.66% within 6 h of the monochromatic light irradiation at 740, 850, 940 and 1100 nm respectively, demonstrating that the as-prepared BiO-OVs photocatalysts also had high mineralization ability under NIR monochromatic light irradiation. The enhanced redox ability of the prepared BiO-OVs heterojunction photocatalysts was further verified by HPLC. As shown in Fig. 18, three obvious peaks could be detected, which were attributed to the RhB molecules (peak a), N, N-diethyl-N'-ethylrhodamine (DER, peak b) and N-ethyl-N'-ethylrhoda-mine (EER, peak c), respectively [79]. For the pure BiO_{2-x}, as show in Fig. 18(a), the intensity of peak a decreased slightly after visible light irradiation for 120 min, demonstrating that only partial RhB molecules were decomposed over the pure BiO_{2-x} photocatalyst. With the decrease of the concentration of RhB, the concentrations of DER and EER species increased firstly and then decreased, indicating that DER and EER were

the main intermediates during the photo-degradation of RhB. However, for BiO-OVs-2 photocatalyst (Fig. 18(b)), after 80 min of visible light irradiation, the RhB molecules were almost completely decomposed over BiO-OVs-2 photocatalyst, which exhibited higher mineralization ability than that of the pure BiO_{2-x} due to the formation of Z-scheme heterojunction between BiO_{2-x} and $Bi_2O_{2.75}$. The HPLC chromatograms of RhB after 360 min of monochromatic light irradiation were shown in the inset of Fig. 18(b). The appearance of peak b and peak c further demonstrated that DER and EED were the main intermediates in RhB decomposition. The mineralization rates of RhB were calculated to be 99.94%, 91.54%, 91.50% and 91.51% after 360 min of 740 nm, 850 nm, 940 nm and 1100 nm monochromatic light irradiation re-spectively, which demonstrated that BiO-OVs-2 heterojunction photo-catalyst also showed strong redox ability under NIR light irradiation, consistent with the results of TOC measurements. The above results

further proved the formation of Z-scheme heterojunction between BiO_{2-x} and $Bi_2O_{2.75}$ owing to the existence of the build-in electric field from the defect sites of Bi atoms to defect sites of O atoms and improved photocatalytic mechanism.

4. Conclusions

In summary, a novel Z-scheme full solar spectrum-driven BiO_{2-x}/$Bi_2O_{2.75}$ heterojunction photocatalyst was successfully fabricated by a simple and facile low-temperature hydrothermal method. The LSPR effect of oxygen vacancy successfully expanded the optical response range of the-prepared photocatalyst to the whole solar spectrum. The formation of Z-scheme heterogeneous interface could boost the separation and migration of photoinduced charge carrier as well as improved redox ability. Bi defects were induced by oxygen vacancy, which was favorable for the molecular oxygen activation and H_2O oxidation. The as-prepared BiO_{2-x}/$Bi_2O_{2.75}$ photocatalyst exhibited enhanced photocatalytic activity compared to the pure BiO_{2-x} and the photodegradation rate of RhB over optimum photocatalyst were 92.68%, 95.79% and 90.34% after visible light/solar light/NIR light irradiation of 40, 20 and 240 min, respectively. Meanwhile, BiO-OVs also exhibited high photocatalytic activity to degrade MO and AR under visible/NIR light irradiation. This work provided a feasible strategy for full solar spectrum degradation of organic dyes.

Appendix A. Supplementary data

Supplementary material related to this article can be found, in the online version, at doi:https://doi.org/10.1016/j.apcatb.2019.04.044.

References

[1] G.M. Neelgund, V.N. Bliznyuk, A. Oki, Photocatalytic activity and NIR laser response of polyaniline conjugated graphene nanocomposite prepared by a novel acid-less method, Appl. Catal. B Environ. 187 (2016) 357–366.

[2] X.L. Hu, J. Tian, Y.J. Xue, Y. Li, H.Z. Cui, Bi_2WO_6 nanosheets decorated with Au nanorods for enhanced near-infrared photocatalytic properties based on surface plasmon resonance effects and wide-range near-infrared light harvesting, ChemCatChem 9 (2017) 1511–1516.

[3] S.W. Cao, J.X. Low, J.G. Yu, M. Jaroniec, Polymeric photocatalysts based on graphitic carbon nitride, Adv. Mater. 27 (2015) 2150–2176.

[4] Y. Zheng, L.H. Lin, B. Wang, X.C. Wang, Graphitic carbon nitride polymers toward sustainable photoredox catalysis, Angew. Chem. Int. Ed. 54 (2015) 12868–12884.

[5] X.L. Hu, X. Liu, J. Tian, Y.J. Li, H.Z. Cui, Towards full-spectrum (UV, visible, and near-infrared) photocatalysis: achieving an all-solid-state Z-scheme between Ag_2O and TiO_2 using reduced graphene oxide as the electron mediator, Catal. Sci. Technol. 7 (2017) 4193–4205.

[6] Q.Z. Zhang, J.J. Deng, Z.H. Xu, M. Chaker, D.L. Ma, High-efficiency broadband C_3N_4 photocatalysts: synergistic effects from upconversion and plasmons, ACS Catal. 7 (2017) 6225–6234.

[7] E. Bilgin Simsek, Solvothermal synthesized boron doped TiO_2 catalysts: photocatalytic degradation of endocrine disrupting compounds and pharmaceuticals under visible light irradiation, Appl. Catal. B Environ. 200 (2017) 309–322.

[8] T. Phongamwong, M. Chareonpanich, J. Limtrakul, Role of chlorophyll in Spirulina on photocatalytic activity of CO_2 reduction under visible light over modified N-doped TiO_2 photocatalysts, Appl. Catal. B Environ. 168–169 (2015) 114–124.

[9] Y.C. Nie, F. Yu, L.C. Wang, Q.J. Xing, X. Liu, Y. Pei, J.P. Zou, W.L. Dai, Y. Li, S.L. Suib, Photocatalytic degradation of organic pollutants coupled with simultaneous photocatalytic H_2 evolution over graphene quantum dots/Mn-N-TiO_2/g-C_3N_4 composite catalysts: performance and mechanism, Appl. Catal. B Environ. 227 (2018) 312–321.

[10] R.R. Hao, G.H. Wang, H. Tang, L.L. Sun, C. Xu, D.Y. Han, Template-free preparation of macro/mesoporous g-C_3N_4/TiO_2 heterojunction photocatalysts with enhanced visible light photocatalytic activity, Appl. Catal. B Environ. 187 (2016) 47–58.

[11] G.H. Dong, L.L. Zhao, X.X. Wu, M.S. Zhu, F. Wang, Photocatalysis removing of NO

[12] X.C. Wang, K. Maeda, X.F. Chen, K. Takanabe, K. Domen, Y.D. Hou, X.Z. Fu, M. Antonietti, Polymer semiconductors for artificial photosynthesis: hydrogen evolution by mesoporous graphitic carbon nitride with visible light, J. Am. Chem. Soc. 131 (2009) 1680–1681.

[13] X.H. Li, J.S. Chen, X.C. Wang, J.H. Sun, M. Antonietti, Metal-free activation of dioxygen by Graphene/g-C_3N_4 nanocomposites: functional dyads for selective oxidation of saturated hydrocarbons, J. Am. Chem. Soc. 133 (2011) 8074–8077.

[14] Y. Park, K.J. McDonald, K.S. Choi, Progress in bismuth vanadate photoanodes for use in solar water oxidation, Chem. Soc. Rev. 42 (2013) 2321–2337.

[15] D.E. Wang, H.F. Jiang, X. Zong, Q. Xu, Y. Ma, G.L. Li, C. Li, Crystal facet dependence of water oxidation on $BiVO_4$ sheets under visible light irradiation, Chem. A Eur. J. 17 (2011) 1275–1282.

[16] P. Chen, L. Chen, Y. Zeng, F. Ding, X. Jiang, N. Liu, C.T. Au, S.F. Yin, Three-dimension hierarchical heterostructure of $CdWO_4$ microrods decorated with Bi_2WO_6 nanoplates for high-selectivity photocatalytic benzene hydroxylation to phenol, Appl. Catal. B Environ. 234 (2018) 311–317.

[17] K. Zhang, J. Wang, W.J. Jiang, W.Q. Yao, H.P. Yang, Y.F. Zhu, Self-assembled perylene diimide based supramolecular heterojunction with Bi_2WO_6 for efficient visible-light-driven photocatalysis, Appl. Catal. B Environ. 232 (2018) 175–181.

[18] X.F. Hu, F. Deng, W.Y. Huang, G.S. Zeng, X.B. Luo, D.D. Dionysiou, The band structure control of visible-light-driven rGO/ZnS-MoS_2 for excellent photocatalytic degradation performance and long-term stability, Chem. Eng. J. 350 (2018) 248–256.

[19] Z.X. Ren, L. Li, B.B. Liu, X.J. Liu, Z. Li, X. Lei, C. Li, Y.Y. Gong, L.Y. Niu, L.K. Pan, Cr (VI) reduction in presence of ZnS/RGO photocatalyst under full solar spectrum radiation from UV/vis to near-infrared light, Catal. Today 315 (2018) 46–51.

[20] Z.Z. Zhang, L. Huang, J.J. Zhang, F.J. Wang, Y.Y. Xie, X.T. Shang, Y.Y. Gu, H.B. Zhao, X.X. Wang, In situ constructing interfacial contact MoS_2/$ZnIn_2S_4$ heterostructure for enhancing solar photocatalytic hydrogen evolution, Appl. Catal. B Environ. 233 (2018) 112–119.

[21] Z.Z. Li, X.C. Meng, Z.S. Zhang, Few-layer MoS_2 nanosheets-deposited on Bi_2MoO_6 microspheres: a Z-scheme visible-light photocatalyst with enhanced activity, Catal. Today 315 (2018) 67–78.

[22] Y. Sun, Z.X. Zhang, A.J. Xie, C.H. Xiao, S.K. Li, F.Z. Huang, Y.H. Shen, An ordered and porous N-doped carbon dot-sensitized Bi_2O_3 inverse opal with enhanced photoelectrochemical performance and photocatalytic activity, Nanoscale 7 (2015) 13974–13980.

[23] Z.T. Liang, Y.L. Cao, Y.Z. Li, J. Xie, N.N. Guo, D.Z. Jia, Solid-state chemical synthesis of rod-like fluorine-doped β-Bi_2O_3 and their enhanced photocatalytic property under visible light, Appl. Surf. Sci. 390 (2016) 78–85.

[24] H.H. Ji, L. Lyu, L.L. Zhang, X.Q. An, C. Hu, Oxygen vacancy enhanced photostability and activity of plasmon-Ag composites in the visible to near-infrared region for water purification, Appl. Catal. B Environ. 199 (2016) 230–240.

[25] D.D. Li, S.H. Yu, H.L. Jiang, From UV to near-infrared light-responsive metal–organic framework composites: plasmon and upconversion enhanced photocatalysis, Adv. Mater. 30 (2018) 1–7.

[26] L.Y. Lin, S. Kavadiya, B.B. Karakocak, Y. Nie, R. Raliya, S.T. Wang, M.Y. Berezin, P. Biswas, ZnO_{1-x}/carbon dots composite hollow spheres: facile aerosol synthesis and superior CO_2 photoreduction under UV, visible and near-infrared irradiation, Appl. Catal. B Environ. 230 (2018) 36–48.

[27] Y. Li, X.Y. Wu, J. Li, K. Wang, G.K. Zhang, Z-scheme g-C_3N_4@Cs_xWO_3 heterostructure as smart window coating for UV isolating, Vis penetrating, NIR shielding and full spectrum photocatalytic decomposing VOCs, Appl. Catal. B Environ. 229 (2018) 218–226.

[28] Y.Y. Zhang, L.L. Wang, X.Y. Kong, H.Y. Jiang, F. Zhang, J.S. Shi, Novel Ag-Cu bimetallic alloy decorated near-infrared responsive three-dimensional rod-like architectures for efficient photocatalytic water purification, J. Colloid Interface Sci. 522 (2018) 29–39.

[29] C.H. Shi, X.L. Dong, J.W. Wang, X.Y. Wang, H.C. Ma, X.F. Zhang, Interfacial defect engineering over fusiform bismuth vanadate photocatalyst enables to excellent solar-to-chemical energy coupling, RSC Adv. 7 (2017) 26717–26721.

[30] X. Xu, X. Ding, X.L. Yang, P. Wang, S. Li, Z.X. Lu, H. Chen, Oxygen vacancy boosted photocatalytic decomposition of ciprofloxacin over Bi_2MoO_6: oxygen vacancy engineering, biotoxicity evaluation and mechanism study, J. Hazard. Mater. 364 (2019) 691–699.

[31] Y.C. Huang, H.B. Li, M.S. Balogun, W.Y. Liu, Y.X. Tong, X.H. Lu, H.B. Ji, Oxygen vacancy induced bismuth oxyiodide with remarkably increased visible-light absorption and superior photocatalytic performance, ACS Appl. Mater. Interfaces 6 (2014) 22920–22927.

[32] X.Y. Kong, Y.Y. Choo, S.P. Chai, A.K. Soh, A.R. Mohamed, Oxygen vacancy induced Bi_2WO_6 for the realization of photocatalytic CO_2 reduction over the full solar spectrum: from the UV to the NIR region, Chem. Commun. 52 (2016) 14242–14245.

[33] X.Y. Liu, G.L. Zhu, X. Wang, X.T. Yuan, T.Q. Lin, F.Q. Huang, Progress in black Titania: a new material for advanced photocatalysis, Adv. Energy Mater. 6 (2016) 1–29.

[34] X.B. Chen, L. Liu, F.Q. Huang, Black titanium dioxide (TiO_2) nanomaterials, Chem. Soc. Rev. 44 (2015) 1861–1885.

[35] J. Li, X.Y. Wu, W.F. Pan, G.K. Zhang, H. Chen, Vacancy-rich monolayer BiO_{2-x} as a highly efficient UV, visible, and near-infrared responsive photocatalyst, Angew. Chem. Int. Ed. 57 (2018) 491–495.

[36] J. Li, J. Wang, G.K. Zhang, Y. Li, K. Wang, Enhanced molecular oxygen activation of Ni^{2+}-doped BiO_{2-x} nanosheets under UV, visible and near-infrared irradiation: mechanism and DFT study, Appl. Catal. B Environ. 234 (2018) 167–177.

[37] Y.F. Jia, S.P. Li, J.Z. Gao, G.Q. Zhu, F.C. Zhang, X.J. Shi, Y. Huang, C.L. Liu, Highly

efficient (BiO)$_2$CO$_3$-BiO$_{2-x}$-graphene photocatalysts: Z-Scheme photocatalytic mechanism for their enhanced photocatalytic removal of NO, Appl. Catal. B Environ. 240 (2019) 241–252.

[38] Q. Hao, R.T. Wang, H.J. Lu, C.A. Xie, W.H. Ao, D.M. Chen, C. Ma, W.Q. Yao, Y.F. Zhu, One-pot synthesis of C/Bi/Bi$_2$O$_3$ composite with enhanced photocatalytic activity, Appl. Catal. B Environ. 219 (2017) 63–72.

[39] M. Jalalah, M. Faisal, H. Bouzid, J.G. Park, S.A. Al-Sayari, A.A. Ismail, Comparative study on photocatalytic performances of crystalline α- and β-Bi$_2$O$_3$ nanoparticles under visible light, J. Ind. Eng. Chem. 30 (2015) 183–189.

[40] M.Y. Xing, J.L. Zhang, F. Chen, B.Z. Tian, An economic method to prepare vacuum activated photocatalysts with high photo-activities and photosensitivities, Chem. Commun. 47 (2011) 4947–4949.

[41] S.X. Yu, Y.H. Zhang, F. Dong, M. Li, T.R. Zhang, H.W. Huang, Readily achieving concentration-tunable oxygen vacancies in Bi$_2$O$_2$CO$_3$: triple-functional role for efficient visible-light photocatalytic redox performance, Appl. Catal. B Environ. 226 (2018) 441–450.

[42] J. Xu, Y.R. Teng, F. Teng, Effect of surface defect states on valence band and charge separation and transfer efficiency, Sci. Rep. 6 (2016) 1–9.

[43] S.L. Wang, Y.L. Mak, S. Wang, J. Chai, F. Pan, M.L. Foo, W. Chen, K. Wu, G.Q. Xu, Visible-near-infrared-light-driven oxygen evolution reaction with noble-metal-Free WO$_2$-WO$_3$ hybrid nanorods, Langmuir 32 (2016) 13046–13053.

[44] J.F. Li, W.T. Li, X.S. Li, Y.H. Li, H. Bai, M.C. Li, G.C. Xi, Plasmonic W$_{18}$O$_{49}$-photosensitized TiO$_2$ nanosheets with wide-range solar light harvesting, RSC Adv. 7 (2017) 23846–23850.

[45] Z.Y. Zhang, J.D. Huang, Y.R. Fang, M.Y. Zhang, K.C. Liu, B. Dong, A nonmetal plasmonic Z-scheme photocatalyst with UV- to NIR-driven photocatalytic protons reduction, Adv. Mater. 29 (2017) 1606688.

[46] X.Y. Kong, W.P.C. Lee, W.J. Ong, S.P. Chai, A.R. Mohamed, Oxygen-deficient BiOBr as a highly stable photocatalyst for efficient CO$_2$ reduction into renewable carbon-neutral fuels, ChemCatChem 8 (2016) 3074–3081.

[47] L.Q. Ye, X.L. Jin, Y.M. Leng, Y.R. Su, H.Q. Xie, C. Liu, Synthesis of black ultrathin BiOCl nanosheets for efficient photocatalytic H$_2$ production under visible light irradiation, J. Power Sources 293 (2015) 409–415.

[48] J.J. Li, B. Weng, S.C. Cai, J. Chen, H.P. Jia, Y.J. Xu, Efficient promotion of charge transfer and separation in hydrogenated TiO$_2$/WO$_3$ with rich surface-oxygen-vacancies for photodecomposition of gaseous toluene, J. Hazard. Mater. 342 (2018) 661–669.

[49] L.P. Zhang, G.H. Wang, Z.Z. Xiong, H. Tang, C.J. Jiang, Fabrication of flower-like direct Z-scheme β-Bi$_2$O$_3$/g-C$_3$N$_4$ photocatalyst with enhanced visible light photoactivity for Rhodamine B degradation, Appl. Surf. Sci. 436 (2018) 162–171.

[50] H. Wang, D.Y. Yong, S.C. Chen, S.L. Jiang, X.D. Zhang, W. Shao, Q. Zhang, W.S. Yan, B.C. Pan, Y. Xie, Oxygen-vacancy-mediated exciton dissociation in biobr for boosting charge-carrier-involved molecular oxygen activation, J. Am. Chem. Soc. 140 (2018) 1760–1766.

[51] G.Q. Zhang, L. Cai, Y.F. Zhang, Y. Wei, Bi^{5+}, Bi$^{(3-x)+}$, and oxygen vacancy induced BiOCl$_x$I$_{1-x}$ solid solution toward promoting visible-light driven photocatalytic activity, Chem. A Eur. J. 24 (2018) 7434–7444.

[52] L. Li, X.G. Feng, Y. Nie, S.G. Chen, F. Shi, K. Xiong, W. Ding, X.Q. Qi, J.S. Hu, Z.D. Wei, L.J. Wan, M.R. Xia, Insight into the effect of oxygen vacancy concentration on the catalytic performance of MnO$_2$, ACS Catal. 5 (2015) 4825–4832.

[53] F. Wang, K. Cao, Y. Wu, G.R. Patzke, Y. Zhou, Electronic and optical properties of N-doped Bi$_2$O$_3$ polymorphs for visible light-induced photocatalysis, J. Mol. Model. 21 (2015) 1–8.

[54] Y.J. Li, F. Yang, Y. Yu, Enhanced photocatalytic activity of α-Bi$_2$O$_3$ with high electron-hole mobility by codoping approach: a first-principles study, Appl. Surf. Sci. 358 (2015) 449–456.

[55] B. Feng, Z.Y. Wu, J.S. Liu, K.J. Zhu, Z.Q. Li, X. Jin, Y.D. Hou, Q.Y. Xi, M.Q. Cong, P.C. Liu, Q.L. Gu, Combination of ultrafast dye-sensitized-assisted electron transfer process and novel Z-scheme system: AgBr nanoparticles interspersed MoO$_3$ nanobelts for enhancing photocatalytic performance of RhB, Appl. Catal. B Environ. 206 (2017) 242–251.

[56] Q.Q. Liu, Y.Q. Xu, J. Wang, M. Xie, W. Wei, L.Y. Huang, H. Xu, Y.H. Song, H.M. Li, Fabrication of Ag/AgCl/ZnFe$_2$O$_4$ composites with enhanced photocatalytic activity for pollutant degradation and E. coli disinfection, Colloids Surf. A Physicochem. Eng. Asp. 553 (2018) 114–124.

[57] S. Ali, H. Granbohm, J. Lahtinen, S.P. Hannula, Titania nanotubes prepared by rapid breakdown anodization for photocatalytic decolorization of organic dyes under UV and natural solar light, Nanoscale Res. Lett. 13 (2018) 179.

[58] P.R. Chowdhury, K.G. Bhattacharyya, Ni/Co/Ti layered double hydroxide for highly efficient photocatalytic degradation of Rhodamine B and Acid Red G: a comparative study, Photochem. Photobiol. Sci. 16 (2017) 835–839.

[59] S. Horikoshi, H. Hidaka, N. Serpone, Environmental remediation by an integrated microwave/UV-illumination method. 1. Microwave-assisted degradation of rhodamine-B dye in aqueous TiO$_2$ dispersions, Environ. Sci. Technol. 36 (2002) 1357–1366.

[60] X.M. Jia, J. Cao, H.L. Lin, M.Y. Zhang, X.M. Guo, S.F. Chen, Transforming type-I to type-II heterostructure photocatalyst via energy band engineering: a case study of I-BiOCl/I-BiOBr, Appl. Catal. B Environ. 204 (2017) 505–514.

[61] F. Chen, Q. Yang, X.M. Li, G.M. Zeng, D.B. Wang, C.G. Niu, J.W. Zhao, H.X. An, T. Xie, Y.C. Deng, Hierarchical assembly of graphene-bridged Ag$_3$PO$_4$/Ag/BiVO$_4$(040) Z-scheme photocatalyst: an efficient, sustainable and heterogeneous catalyst with enhanced visible-light photoactivity towards tetracycline degradation under visible light irradiation, Appl. Catal. B Environ. 200 (2017) 330–342.

[62] Y. Nosaka, A.Y. Nosaka, Generation and detection of reactive oxygen species in photocatalysis, Chem. Rev. 117 (2017) 11302–11336.

[63] H. Li, J. Li, Z.H. Ai, F.L. Jia, L.Z. Zhang, Oxygen vacancy-mediated photocatalysis of BiOCl: reactivity, selectivity, and perspectives, Angew. Chem. Int. Ed. 57 (2018) 122–138.

[64] J.L. Zhang, Y. Lu, L. Ge, C.C. Han, Y.J. Li, Y.Q. Gao, S.S. Li, H. Xu, Novel AuPd bimetallic alloy decorated 2D BiVO$_4$ nanosheets with enhanced photocatalytic performance under visible light irradiation, Appl. Catal. B Environ. 204 (2017) 385–393.

[65] W.J. He, Y.J. Sun, G.M. Jiang, H.W. Huang, X.M. Zhang, F. Dong, Activation of amorphous Bi$_2$WO$_6$ with synchronous Bi metal and Bi$_2$O$_3$ coupling: photocatalysis mechanism and reaction pathway, Appl. Catal. B Environ. 232 (2018) 340–347.

[66] H.W. Huang, S.C. Tu, C. Zeng, T.R. Zhang, A.H. Reshak, Y.H. Zhang, Macroscopic polarization enhancement promoting photo- and piezoelectric-induced charge separation and molecular oxygen activation, Angew. Chem. Int. Ed. 56 (2017) 11860–11864.

[67] P.P. Das, A. Roy, M. Tathavadekar, P.S. Devi, Photovoltaic and photocatalytic performance of electrospun Zn$_2$SnO$_4$ hollow fibers, Appl. Catal. B Environ. 203 (2017) 692–703.

[68] C.C. Zhao, G.Q. Tan, J. Huang, W. Yang, H.J. Ren, A. Xia, Preparation of self-assembled spherical g-C$_3$N$_4$/tz-Bi$_{0.92}$Gd$_{0.08}$VO$_4$ heterojunctions and their mineralization properties, ACS Appl. Mater. Interfaces 7 (2015) 23949–23957.

[69] Y.C. Deng, L. Tang, C.F. Feng, G.M. Zeng, Z.M. Chen, J.J. Wang, H.P. Feng, B. Peng, Y.N. Liu, Y.Y. Zhou, Insight into the dual-channel charge-charrier transfer path for nonmetal plasmonic tungsten oxide based composites with boosted photocatalytic activity under full-spectrum light, Appl. Catal. B Environ. 235 (2018) 225–237.

[70] A.Y. Shi, H.H. Li, S. Yin, J.C. Zhang, Y.H. Wang, H$_2$ Evolution over g-C$_3$N$_4$/Cs$_x$WO$_3$ under NIR light, Appl. Catal. B Environ. 228 (2018) 75–86.

[71] P.X. Qiu, C.M. Xu, H. Chen, F. Jiang, X. Wang, R.F. Lu, X.R. Zhang, One step synthesis of oxygen doped porous graphitic carbon nitride with remarkable improvement of photo-oxidation activity: role of oxygen on visible light photocatalytic activity, Appl. Catal. B Environ. 206 (2017) 319–327.

[72] L.B. Jiang, X.Z. Yuan, G.M. Zeng, J. Liang, X.H. Chen, H.B. Yu, H. Wang, Z.B. Wu, J. Zhang, T. Xiong, In-situ synthesis of direct solid-state dual Z-scheme WO$_3$/g-C$_3$N$_4$/Bi$_2$O$_3$ photocatalyst for the degradation of refractory pollutant, Appl. Catal. B Environ. 227 (2018) 376–385.

[73] Y.Q. Cui, X.Y. Zhang, R.N. Guo, H.X. Zhang, B. Li, M.Z. Xie, Q.F. Cheng, X.W. Cheng, Construction of Bi$_2$O$_3$/g-C$_3$N$_4$ composite photocatalyst and its enhanced visible light photocatalytic performance and mechanism, Sep. Purif. Technol. 203 (2018) 301–309.

[74] L. Mao, X.Y. Cai, S.Q. Yang, K.L. Han, J.Y. Zhang, Black phosphorus-CdS-La$_2$Ti$_2$O$_7$ ternary composite: effective noble metal-free photocatalyst for full solar spectrum activated H$_2$ production, Appl. Catal. B Environ. 242 (2018) 441–448.

[75] O. Elbanna, P. Zhang, M. Fujitsuka, T. Majima, Facile preparation of nitrogen and fluorine codoped TiO$_2$ mesocrystal with visible light photocatalytic activity, Appl. Catal. B Environ. 192 (2016) 80–87.

[76] R. Liu, L.N. Ma, G.D. Niu, X.L. Li, E.N. Li, Y. Bai, G.H. Yuan, Oxygen-deficient bismuth oxide/graphene of ultrahigh capacitance as advanced flexible anode for asymmetric supercapacitors, Adv. Funct. Mater. 27 (2017) 1–9.

[77] S. Wang, P. He, L.P. Jia, M.Q. He, T.H. Zhang, F.Q. Dong, M.Z. Liu, H.H. Liu, Y. Zhang, C.X. Li, J. Gao, L. Bian, Nanocoral-like composite of nickel selenide nanoparticles anchored on two-dimensional multi-layered graphitic carbon nitride: a highly efficient electrocatalyst for oxygen evolution reaction, Appl. Catal. B Environ. 243 (2019) 463–469.

[78] K.Q. Liang, C.G. Wang, X.J. Xu, J.C. Leng, H. Ma, Capacitive and photocatalytic performance of Bi$_2$S$_3$ nanostructures synthesized by solvothermal method, Phys. Lett. Sect. A Gen. At. Solid State Phys. 381 (2017) 652–657.

[79] P.X. Lei, C.C. Chen, J. Yang, W.H. Ma, J.C. Zhao, L. Zang, Degradation of dye pollutants by immobilized polyoxometalate with H$_2$O$_2$ under visible-light irradiation, Environ. Sci. Technol. Lett. 39 (2005) 8466–8474.